Doctorate Dissertation

博士論文

Search for Neutrinos associated with Gamma-ray Bursts in Super-Kamiokande

(スーパーカミオカンデにおける
ガンマ線バーストに伴うニュートリノ探索)

A Dissertation Submitted for Degree of Doctor of Philosophy

December 2018

平成 30 年 12 月博士(理学)申請

Department of Physics, Graduate School of Science,

The University of Tokyo

東京大学大学院理学系研究科物理学専攻

Orii Asato

織井　安里

Search for Neutrinos associated with Gamma-ray Bursts in Super-Kamiokande

A. Orii

February 21, 2019

Abstract

Gamma-Ray Bursts (GRBs) are one of the most luminous astronomical objects. Though satellites and ground telescopes have observed some features, much of their mechanism is still not confirmed. We searched for neutrinos associated with GRBs in the Super-Kamiokande (SK) detector.

From Dec. 2008 to Mar. 2017, 2208 GRbs occurred during SK normal data-taking periods. In a search window of $\pm$500 sec around each GRB trigger time, 250 events remained after reduction with an expected background rate of 0.114 events/1000 seconds. The time distribution of the number of events and energy distribution of combined data does not show significant excess over the background.

For individual GRBs, 3 or less SK events were detected in the search window. The only GRB with 3 SK events is GRB140616A. The 3 SK events may be events caused by cosmic ray muons.

The number of SK events between GRB start/stop time (N_{ev}) observed by satellites and telescopes are also studied. From toy Monte Carlo simulation, the distribution of N_{ev} was evaluated as consistent with background.

Assuming a flat spectrum, the fluence limit was calculated. The fluence limit from 8 MeV to 100 MeV for all 2208 GRBs is $1.03 \times 10^{8} \mathrm{cm}^{-2}$. The limit as a function of energy was calculated and is $3.4 \times 10^{9} \mathrm{cm}^{-2}$ at 12 MeV.

Contents

1 Introduction

Gamma-Ray Bursts (GRB) are luminous explosions in Universe. Enormous energy is released in gamma-rays in a short time. After their 1967 discovery, much research revealed their features, though still their mechanism is not clear.

Neutrinos interact less than photons. If a GRB is observed through neutrinos, the information would be helpful.

The 2017/10/7 observation of GW170917 was reported in [3]. This event was also observed as a short GRB. Follow-up observations by ground telescope determined its progenitor to be a neutron star-neutron star merger event.

1.1 Neutrinos

The neutrino was predicted by Pauli in 1930 to conserve momentum in beta decays. It was experimentally observed in 1956 by Reines and Cowan. Originally, neutrinos were thought to be massless. Now, it is known that they have mass due to the observation of neutrino oscillation. They have 3 flavors corresponding to the leptons. Because their mass eigenstate and flavor eigenstate is different, the flavor oscillates or changes during travel.

In the Standard Model, the neutrino is a fundamental particle. The interaction by gravity is negligible due to its small mass. It is electrically neutral and does not interact with the strong force. The weak nuclear force is the main interaction channel. Neutrinos pass through massive objects with little interaction. Its experimental study needs a large detector and sophisticated techniques.

Neutrinos are generated via nuclear reactions like fusion in the sun, fission in the Earth's crust and mantle, and in reactors. Neutrinos are also generated when a cosmic ray interacts with a nucleus in the atmosphere, creating unstable particles that decay. There are also artificial neutrino beams. Neutrino properties have been studied from these various sources.

Neutrinos can also be used for studying astronomical events. Many astronomical events make or are predicted to make large amounts of neutrinos. Because of its small interaction rate, neutrinos can bring different information to the Earth without the effect of scattering or shielding. The only currently observed astronomical neutrinos are from the sun and from supernova 1987A. This thesis is the result of the search for neutrinos from gamma-ray bursts.

1.2 Gamma-Ray Burst

Gamma-ray bursts (GRB) are one of the most luminous astronomical object ever observed. The observed energy of GRBs distribute from high energy gamma-rays

to radio. GRBs comes from random directions without notice. During the prompt phase, typical GRBs are more luminous than the rest of the gamma-rays in the sky.

Assuming isotropic emission, the released energy is 10^{54} erg. However, In fact, gamma-ray emission is a directional beam. Therefore, the total gamma-ray energy of a GRB is much less and comparable to a supernova. GRBs are categorized as long GRBs or short GRBs depending on the duration of the gamma-ray. Long GRBs have durations longer than 2 sec and short GRBs less than 2 sec.

1.2.1 Observation

GRBs are observed about once a day in the entire sky on average. After an observation of gamma-rays by the satellites, the afterglow of X-ray, optical ray, or radio is observed by follow-up ground telescopes. The redshift of the afterglow enables determination of the distance and host galaxy. The progenitor is at a cosmological distance.

Their gamma radiation is non-thermal and can be usually characterized by a Band function[18]. The function is made of two smoothly joined power-laws (Fig. 1). For some GRBs, a small thermal component is observed.

The duration of GRBs (Fig. 2) have 2 peaks, one at 30 sec and the other at 0.3 sec. Most of the GRBs have durations between 0.1 sec to 1000 sec.

The light curves of GRBs have various time development (Fig. 3. The bursts have features like a single peak with a fast rise exponential decay (FRED), erratic multi peaks, and long quiet periods between peaks.

After the prompt gamma-ray signal, a longer signal called afterglow is observed. The observed afterglows have a power-law energy spectrum from x-ray to radio. They decay as a power-law function of time. Fig. 4 shows the time development of 30 afterglows before the launch of Swift. Most of the x-ray afterglows disappear as a power-law with exponent $\sim$1.2.

More features were observed by the rapid follow-up of the ground telescope with Swift. The schematic features are shown in Fig. 5. The rapid decay of many bursts is consistent with the low energy tail of the prompt gamma-ray. The continuous injection of the fireball energy into the interstellar medium (ISM) is thought to cause the shallow decay after this rapid decay. The exponent of the shallow decay is $\sim$0.5. The continued activity of the fireball makes x-ray flares.

1.2.2 Model

Gamma rays are emitted from the relativistic fireball. The fireball model is confirmed by the observation of the afterglow[33, 51, 45]. In the fireball model, the GRB is

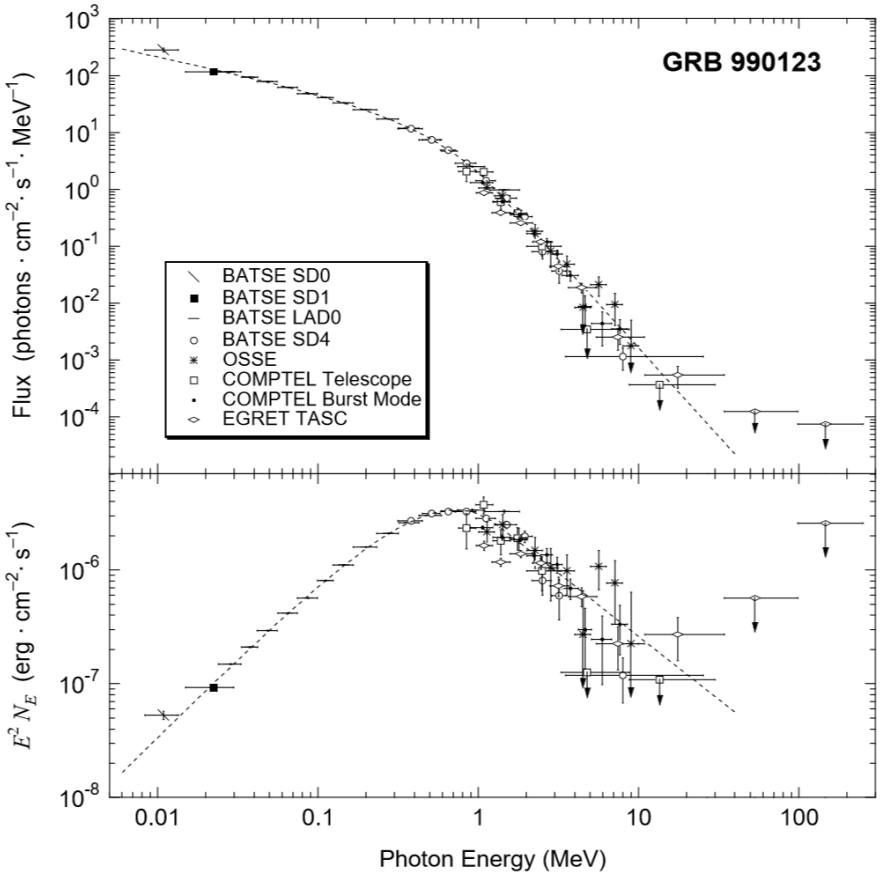

Figure 1: The spectra of GRB990123 from the Compton Gamma-ray Observatory. The top panel shows photon flux and the bottom shows the energy flux. Figure from [24].

generated when relativistic ejecta slow down by interactions with the external mass or another layer of the ejecta. Neutrinos are also generated by this process.

As the central engine, different models are widely accepted for long GRBs and short GRBs. The model for long GRBs is the rotating core of the massive star that decays into a neutron star (NS) or a black hole (BH)[38]. The model for short GRBs is the merger of a NS or BH[38].

The neutrino energy and flux depend on the model of the central engine and that of neutrino generation. The primary neutrino production interactions of the fireball model are $p-\gamma$ interactions ($E_\nu \sim 10^{14}10^{19}\ eV$or higher)[52, 20, 29, 53, 51] or $p-n$ collisions (E_ν ∼10 MeV-10 GeV)[52, 20, 8, 42, 37].

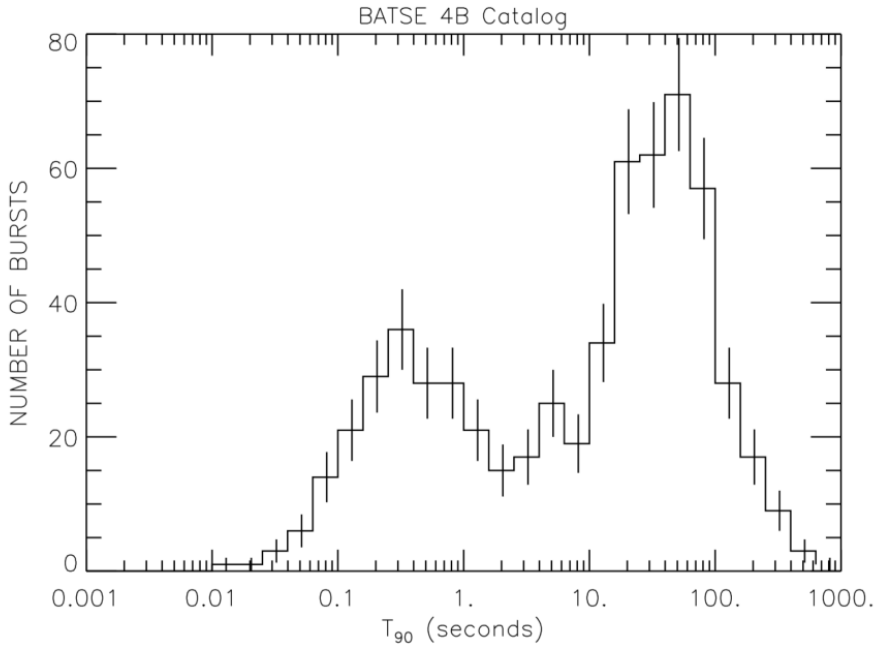

Figure 2: The duration of GRBs in the 4th BATSE catalog. Figure from [26].

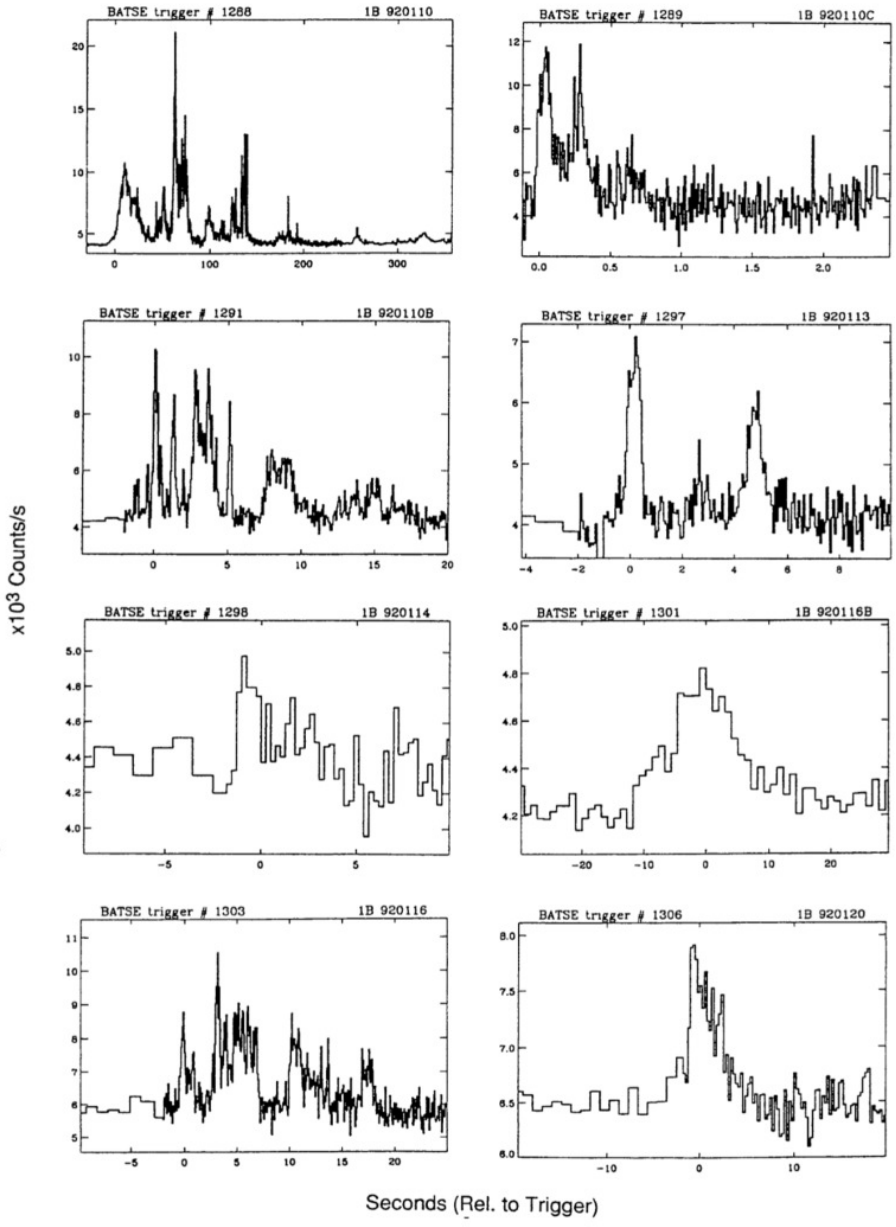

Figure 3: The light curves of 8 bursts observed by BATSE. Figure from [27].

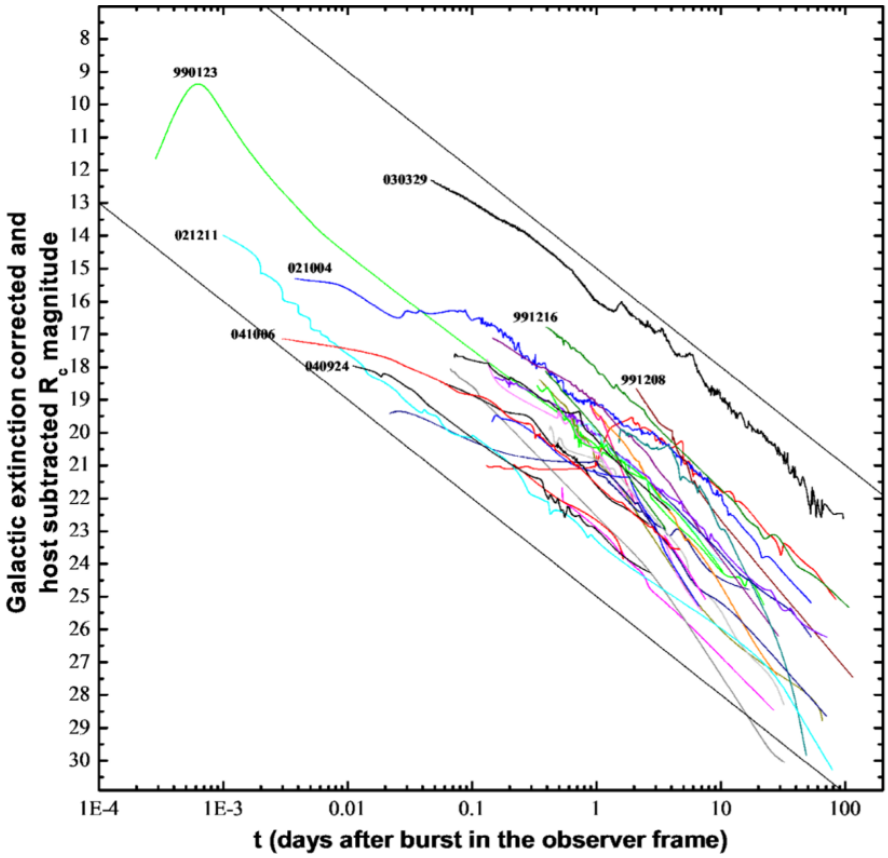

Figure 4: The observed near infrared afterglow from [32]. The two black line correspond to decay slopes of $\alpha = 0.5$.

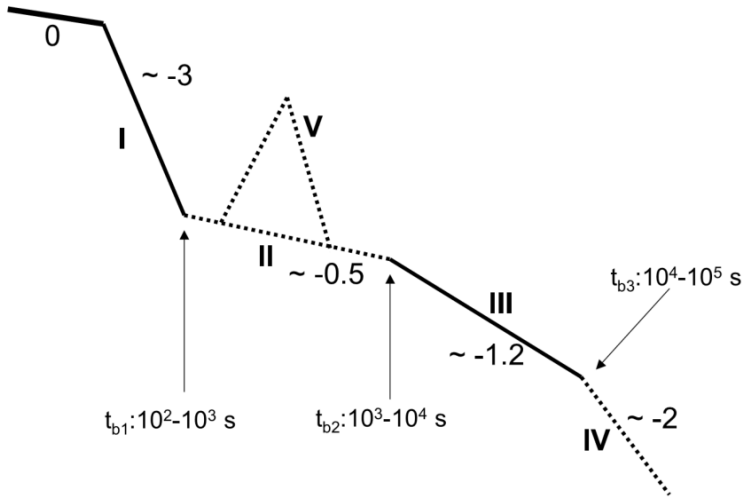

Figure 5: The schematic features observed in early x-ray afterglows with Swift[17].

1.2.3 MeV Neutrinos from GRBs

In the fireball scenario, the neutrino fluence is estimated as [31],

$$\Phi_\nu = \left(\frac{\mathrm{E}_{\nu,\mathrm{tot}}}{2\times 10^{53}\ \mathrm{erg}}\right)\left(\frac{65\ \mathrm{MeV}}{\mathrm{E}_\nu}\right)\left(\frac{4000\ \mathrm{Mpc}}{\mathrm{D}}\right)^2 \mathrm{cm}^{-2}, \tag{1}$$

where $\mathrm{E}_{\nu,\mathrm{tot}}$ is the total energy in the fireball, E_ν is average neutrino energy, and D is the distance to a GRB. For a GRB of typical energy at redshift z = 2, $\Phi_\nu \sim 1\ \mathrm{cm}^{-2}$ for several tens of MeV neutrinos. This estimated fluence is much smaller than the fluence limit of MeV neutrinos given by the previous study with Super-Kamiokande[28] is $10^5 - 10^8\ \mathrm{cm}^{-2}$.

However, a larger fluence of low energy neutrinos is predicted with a cosmic string scenario than with a fireball scenario. Cosmic strings are linear defects predicted in most grand unified models. At a symmetry breaking phase transition in the early universe, cosmic strings could be formed as thin superconducting wires that respond to external electromagnetic fields[10]. Cosmic strings models can give a better explanation to the following:

- The high-redshift GRBs, GRB 080913, and GRB 090423 have short durations but have high energy release, typical for long GRBs.
- The rate of high-redshift GRBs is larger than the predicted rate by the collapsar model with an ordinary star formation rate[11].

The estimated neutrino fluence is[31],

$$\Phi_\nu = 10^8 \left(\frac{\eta_\nu}{10^{-10}}\right)^{-1} \left(\frac{E_{\nu obs}}{100\mathrm{MeV}}\right)^{-1} \left(\frac{F_\gamma}{10^{-6}\mathrm{ergcm}^{-2}}\right) \mathrm{cm}^{-2}, \quad (2)$$

where η_ν is the ratio of gamma-gay energy release to that of the neutrino, $E_{\nu \mathrm{obs}}$ is the average neutrino energy and F_ν is fluency in photons. $\Phi_\nu \sim 10^7 - 10^8 \mathrm{cm}^{-2}$ is estimated with same condition GRB to that of fireball model.

The prediction of neutrino fluence limit differs much depending on models. The neutrino search with SK will help to constrain the model.

1.3 Previous Experimental Searches

Until now, no clear neutrino signal is observed in GRBs. The following is a summary of the previous experimental searches. Fig. 6 shows the fluence limit.

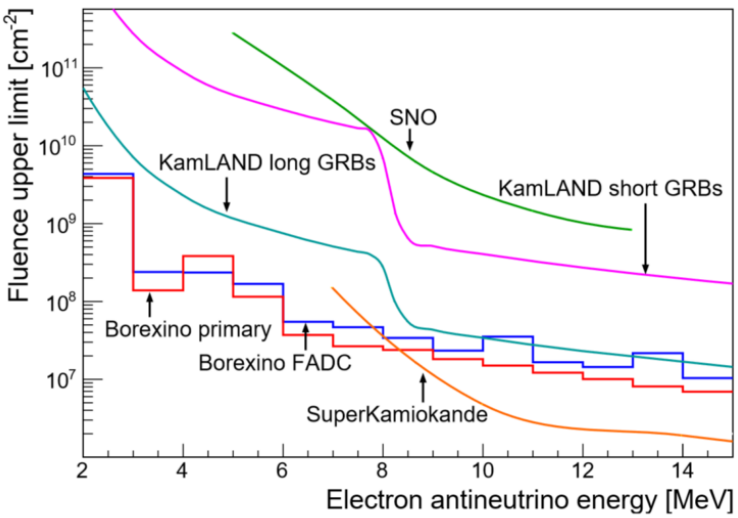

Figure 6: Fluence upper limits for electron antineutrinos from GRBs at low energy. Figure from [22].

- SK-I
  The correlation with 1454 GRBs from April, 1996 to May, 2000 was searched[28]. The solar neutrino, atmospheric neutrino and up-going muon sample was used. Their energy is 7 MeV to 100 TeV.

  After this, the search for the bright GRB, GRB080319B is done[19].

- Kamland
  Kamland is a liquid scintillator detector[21]. The data period from Aug. 2002 to Jun. 2013 is divided into Period I and II by the condition of the reactors. In Period I, 7.5 MeV to 100 MeV neutrinos were searched for in 192 GRBs. In Period II, 0.9 MeV to 100 MeV neutrino were searched for in 39 GRBs.

- Borexino[22]
  Borexino is also a liquid scintillator detector. It searches $\bar{\nu_e}$ via inverse beta decay and all flavors via the scattering on electrons.

  The neutrinos correlated with 2,350 GRB from Dec. 2007 to Nov. 2015 was searched. The target energy range is from 1.8 MeV to 15 MeV.

- IceCube
  IceCube, a Cherenkov detector, searched the TeV and PeV range of neutrino for 1172 GRBs from May 2010 to May 2015.

- ANITA[13]
  ANITA is a balloon experiment which searches for radio emission from electromagnetic showers by the interaction of ultra-high energy neutrino with the antarctic ice sheet. During 31 days of the second flight of ANITA, 26 GRBs are observed by Swift or Fermi. The fluence limit of $10^8 - 10^{12}$ GeV is calculated.

- ANTARES
  ANTARES is a water Cherenkov detector in the Mediterranean sea. It searched neutrinos with energies of TeV to PeV for 40 GRBs in 2007[5] and 296 GRBs in 2007 to 2011[6].

- SNO[16]
  The SNO detector is a Cherenkov detector of heavy water in Sudbury's Creighton mine. The neutrino is typically below 20 MeV around 190 GRBs are searched.

- BUST[36]
  BUST, Bakusan Underground Scintillation Telescope searched for 20-100 MeV neutrinos during 97 GRBs in 2012.

2 The Super-Kamiokande Detector

2.1 Detector Overview

Super-Kamiokande (SK) is a 50 kton water Cherenkov detector located in the Kamioka mine. Cosmic ray muons are reduced by 1,000 m rock (2700 m.w.e.) shield. The detector has a cylindrical shape with a diameter of 39.3 m and height of 41.4 m.

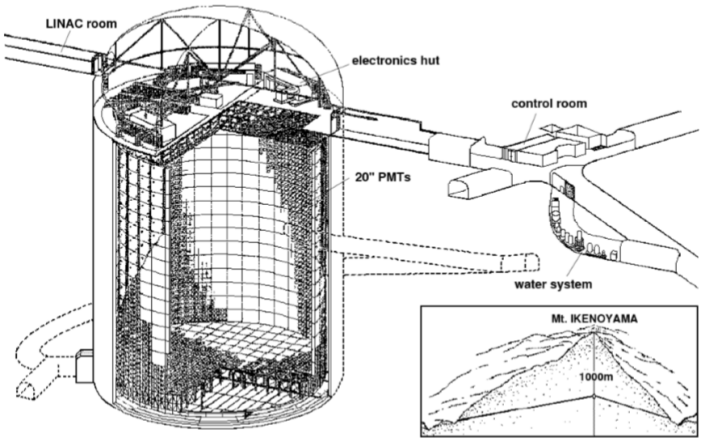

Figure 7: Schematic view of the SK detector.

A stainless steel frame structure divides the detector into two volumes, an inner detector (ID) and outer detector (OD). The structure forms an optical barrier and support for photo-multiplier tubes (PMTs). In the OD, 1,885 8inch PMTs monitor particles entering from outside and 2.5 m of water shields gamma-rays from the rock surrounding the detector. Tyvek sheet which surround the outer side of the frame structure increase the veto sensitivity.

The inner side of the frame structure is surrounded by polyethylene terephthalate black sheet to reduce optical reflections. The ID is monitored by 11,129 20 inch PMTs providing a photo-coverage of $\sim$40%.

The volume within 2 m from the ID wall is not used for low energy analysis due to too many background events. The remaining 22.5 kton volume is called the fiducial volume (FV). The space above the detector is a research dome with 4 electronics huts and a central control room.

SK has five observation phases:

1. SK-I started observation on April, 1996. This period ended on July, 2001.

2. After regular maintenance in July, 2001, a shock wave from the implosion of a PMT caused the chain implosion of almost half of the PMTs. Then, the remaining PMTs were re-distributed and SK-II started on October, 2002. From SK-II, PMTs are protected from shock waves by acrylic covers and fiberglass reinforced plastic (FRP). SK-II was stopped to mount new PMTs on October, 2005.

3. After the PMT mounting work, SK-III started on June, 2006.

4. In August, 2008, new electronics and data acquisition system was installed, ending SK-III and beginning SK-IV. SK-IV was stopped for tank refurbishment work from May, 2018.

5. The work finished in January, 2019, beginning SK-V. Gadolinium sulfate will be added to the water later during this phase.

2.2 Detection Principle

SK detects Cherenkov light, which is emitted when a charged particle travels faster than the speed of light in the medium. Cherenkov light is radiated with a cone pattern along the path of the charged particle.

The angle between the direction of the charged particle and that of the Cherenkov light is called the Cherenkov angle θ_c and is calculated by

$$\cos\theta_c = \frac{1}{\beta n(\lambda)}, \tag{3}$$

where β is the speed of the charged particle relative to light speed in vacuum and $n(\lambda)$ is the refractive index at the wavelength λ. In pure water, the refractive index at 589 nm is 1.33. For the ultra relativistic particles like electrons and positrons, θ_c is 42°. In the energy range of interest, heavier particles like muons and pions have a smaller Cherenkov angle.

The energy threshold for emitting Cherenkov light is determined by

$$E_{thr} = \frac{m}{\sqrt{(1-(1/n)^2)}}, \tag{4}$$

where m is the rest mass of the charged particle.

The number of Cherenkov photons along the trajectory per wavelength is calculated by

$$\frac{d^2N}{d\lambda dx} = \frac{2\pi z^2\alpha}{\lambda^2}(1-\frac{1}{\beta^2 n^2(\lambda)}) = \frac{2\pi z^2\alpha}{\lambda}\sin^2\theta_c, \tag{5}$$

where z is the particle charge in units of e and α is the fine structure constant.

2.3 Photomultiplier Tubes

The 20-inch PMT (R3600) [15] for the ID was developed by Hamamatsu Photonics. The schematic is shown in Fig. 8.

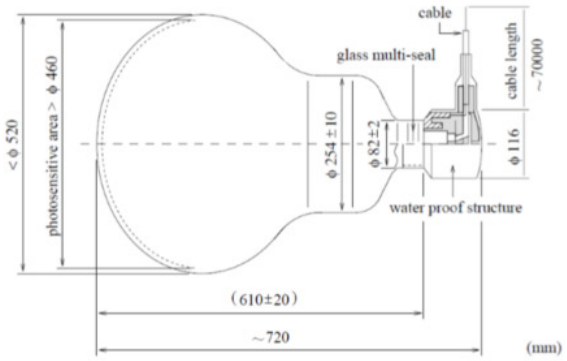

Figure 8: A schematic of the Hamamatsu R3500 PMT.

Its photo-cathode is made from bailkali (Sb-K-Cs) and is sensitive to photons of wavelength 300∼600 nm. Its quantum efficiency is about 20% at maximum (Fig. 9). A photo-electron (p.e.) generated through the photoelectric effect is amplified by 10^7 through the chain of dynodes. The PMT dark noise is 4 kHz. The earth magnetic field, which affects the PMT response, is reduced from 450 mG to 50 mG by Helmholtz coils surrounding the detector.

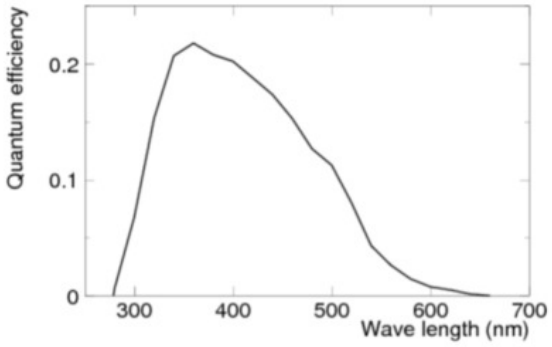

Figure 9: The quantum efficiency of the Hamamatsu R3600 as a function of wavelength.

2.4 Water Systems

The water purification system (Fig. 10) was developed to maintain the quality of water transparency and radioactivity. The higher transparency gives less attenuation of the Cherenkov light. Radioactivity can produce backgrounds in the low energy analysis.

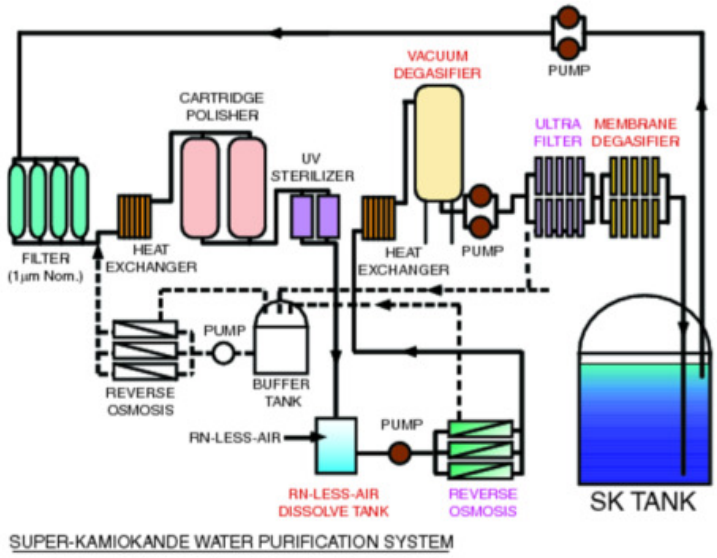

Figure 10: The SK water purification system.

The water system consists of the following components:

- 1 μm filter:
  Removes large particles.
- Heat exchanger:
  Maintains the water temperature at 13°. Water temperature variations cause convection, while higher temperatures increase PMT dark noise and the growth of bacteria.
- Cartridge polisher:
  Removes heavy ions.
- UV sterilizer:
  Kills bacteria.
- Vacuum de-gasifier:
  Removes oxygen and radon in water.

- Ultra filter:
  Removes particles larger than 10 nm.
- Membrane de-gasifier:
  Removes dissolved gas.
- Reverse osmosis:
  Removes large particles with molecular weight > 100.

The water circulates at 60 tons per hour. Due to heat from the PMTs, the water becomes hot as it remains in the tank. It is filled from the bottom of the detector and drained from the top (Fig. 11).

The water temperature is monitored in the ID and OD. It is uniform from the bottom to 11 m below the center and slightly increases with height (Fig. 12). The difference between top and bottom is 0.2 °C.

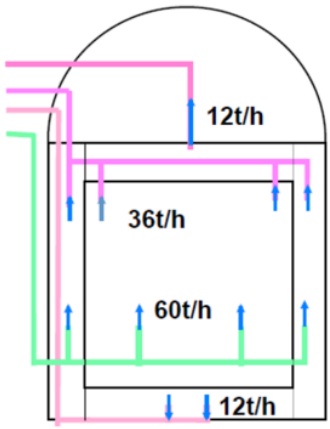

Figure 11: The SK water flow.

2.5 Radon Free Air Systems

The air in the mine includes radon from the surrounding rocks. Radon affects the low energy background rate and workers' health. SK has a system that takes air from outside the mine and reduces radon in the air. A schematic view of the radon free air system is shown in Fig. 13 and consists of the following components:

- Compressor:
  Provides air pressure up to 7-8.5 atm.

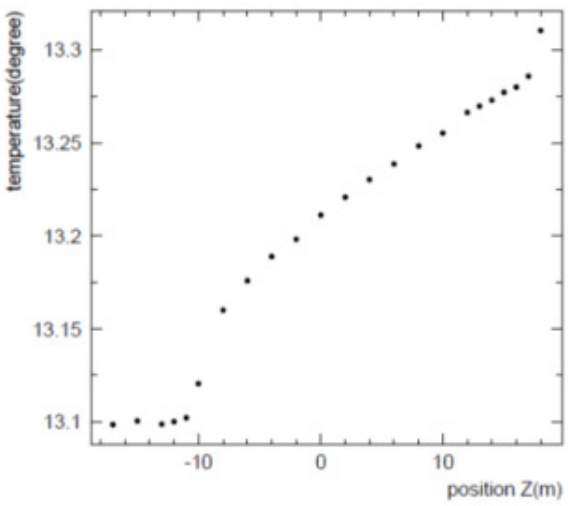

Figure 12: The z-dependence of the water temperature.

- Air filter:
  Removes dust in the air. The air goes through 3 types of filters, 0.3 μm, 0.1 μm, and 0.01 μm, from large to small.
- Air drier:
  Removes water and CO_2 in the air.
- Carbon column:
  Absorbs the radon in the air. 8 m^3 of charcoal is used in total.
- Cooled charcoal:
  Has better random removal efficiency. The volume is 50 L.

The radon level increases to $\sim$2000 Bq/m^3 in the summer and decreases to $\sim$260 Bq/m^3 in the winter. The radon free air system maintains $\sim$40 Bq/m^3 in the experimental area. The radon free air in the tank keeps higher pressure (0.3 kPa) than the outside of the tank. This prevents the air with radon in the mine from getting into the tank.

2.6 Front-end Electronics and Data Acquisition System

The front-end electronics and data acquisition system (DAQ) was upgraded in August, 2008. This upgrade enables more stable data taking and larger data throughput.

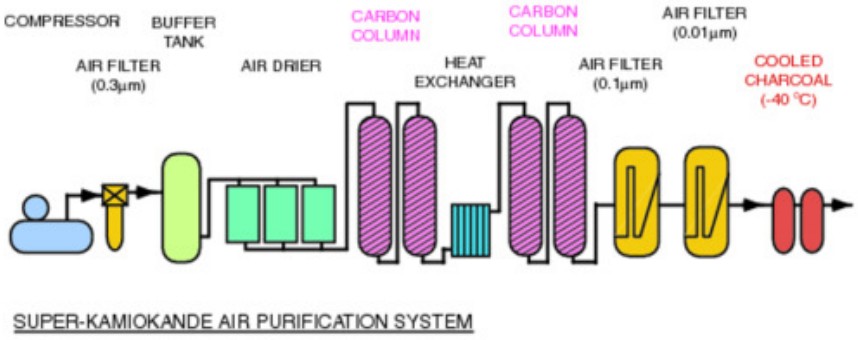

Figure 13: The radon free air system

Each PMT hit is recorded without loss and selected by a software trigger. Since SK has various physics purposes, several types of software triggers were installed. The low energy (LE) trigger, the high energy (HE) trigger, and the super high energy (SHE) trigger have a 40-μs timing window. 5 μs before the trigger is stored for pre-activity gamma studies and the following 35 μs is for post-activity studies. The trigger threshold is 47, 50, and 70 hits in 200 nsec for LE, HE, and SHE, respectively, at the beginning of the new DAQ period. The SHE threshold was changed to 58 hits in the summer of 2011.

Fig. 14 shows the schematic of the new DAQ system. The signals from PMTs go to the new front-end electronics, QTC (charge-to-time converter) Based Electronics with Ethernet (QBEE, Fig. 15). The QBEE has a 24 analog input channel with a dynamic range of 0.2 to 2500 pC. It works 5-times faster than the previous electronics [1]. 8 QTC chips mounted in the QBEE integrate the input charge and output a pulse of proportional width. The pulse width and timing is digitized by a time-to-digital converter (TDC). The digital information is processed by a Field Programmable Gate Array (FPGA) [30].

The TCP packets of data from 500 QBEEs are sent to the 20 front-end PCs. The front-end PCs sort the data in time and send the data to 10 merger PCs. The merger PCs also sort the data in time and then, apply the event building process to the data in the same time region. In the event building process, the data from 20 front-end PCs is scanned by the software trigger. The triggered events are sent to the organizer PC and recorded on disk. The Gigabit Ethernet is used for data transfer between PCs.

Since the new DAQ can handle large throughput, it can record events at a high trigger rate. The high trigger rate is caused by the lower trigger threshold or high rate burst such as a supernova at the distance of the galactic center ($\sim$8.5 kpc).

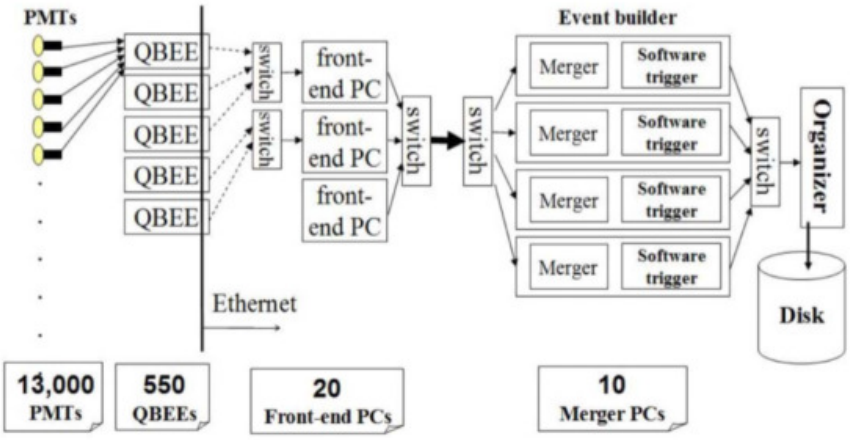

Figure 14: The schematic of the DAQ system.

For a much higher trigger rate target like a nearby supernova (Betelgeuse, ∼200 pc), a DAQ system that records the number of hit PMTs was installed[44]. The QTC on QBEE outputs the digital hitsum, the number of hit PMTs within ∼17 nsec. This DAQ makes 2 types of hitsums, a 60 MHz sum and 60 kHz sum. The 60 MHz sum is the sum of the digital hitsum for all QBEEs and recorded only when a high rate event occurs. The 60 kHz sum is the sum of the 60 MHz sum in 17 μs and used to monitor the hit rate. This DAQ system enables to record the time development of the total energy deposit.

2.7 Monitoring system

The condition of data taking is monitored by various tools. The "slow control" monitor checks the status of the high voltage and the temperature of the electronics. The data stream, the PMT conditions, and the trigger rate are monitored by the process making their distributions. The data transfer and the offline process is also monitored. The online display program shows the visual image of an event in real time. The display helps to monitor the DAQ system and the PMTs.

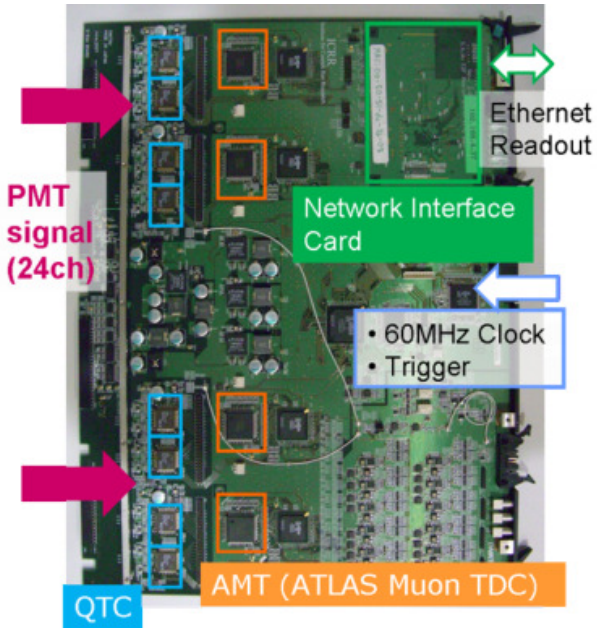

Figure 15: QBEE.

3 Detector Calibration

3.1 PMT Calibration

PMT calibration is necessary for interpreting the recorded charge and timing. First, the high voltage on each PMT is tuned to make the response of all PMTs almost uniform. Then, the PMT gain is measured to convert ADC counts to number of photo-electrons (p.e.). The relative hit timing between PMTs is also corrected.

3.1.1 Absolute Gain

The global absolute gain, a conversion factor from pC to p.e., is measured with a Ni-Cf source. As the γ-rays from this source are about 9 MeV, almost all of the PMT hits are caused by single photons. The absolute gain is derived from the average charge distribution of single photons.

3.1.2 Relative Gain

The relative gain of PMTs is determined by a laser system. The system has a laser of high intensity and low intensity. The charge of the i-th PMT for the high intensity laser is given by:

$$Q_{obs}(i) \propto I_{high}(i) \times QE(i) \times G(i) \tag{6}$$

and for low intensity:

$$M_{hit}(i) \propto I_{low}(i) \times QE(i), \tag{7}$$

where $I_{high/low}$ is the light intensity expected at the i-th PMT for high and low intensities, respectively. $QE(i)$ is the quantum efficiency and $G(i)$ is the relative gain. The ratio of two equation is:

$$G(i) = \frac{Q_{obs}(i)}{M_{hit}(i)} \times \frac{I_{low}(i)}{I_{high}(i)}. \tag{8}$$

The effect of attenuation in water and geometry is canceled out in the ratio. Namely, the $I_{low}(i)/I_{high}(i)$ is common for all PMTs, such that

$$G(i) \propto \frac{Q_{obs}(i)}{N_{obs}(i)}. \tag{9}$$

Fig. 16 shows the obtained relative gain. From absolute and relative gain, the ADC count is converted to p.e.

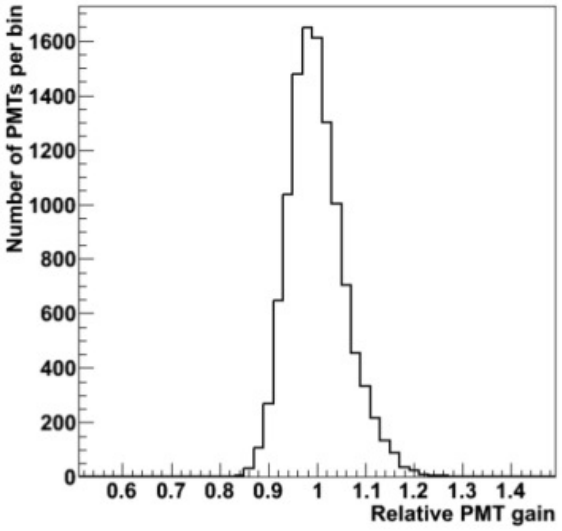

Figure 16: The distribution of relative PMT gains.

3.1.3 Timing

The relative timing is important for vertex reconstruction. The variation of timing is caused by differences in PMT transit time and cable length. Furthermore, when the observed charge is different, the timing also changes due to the slewing effect of the discriminator.

The timing calibration is performed with a N_2 laser. wavelength of N_2 laser is shifted to 398 nm by a dye. Via a optical fiber, the N_2 laser goes into a diffuser ball in the center of the SK tank. The light intensity is changed by optical filters and the response for several pulse height is measured. Fig. 17 is the typical "TQ-map", a 2-D plot of PMT timing versus pulse height. The TQ-map is made for each PMT individually.

The global timing resolution is calculated from the residual timing difference of PMT hits with the TQ-map. For single photo-electrons, the global timing resolution is 3 ns. The global timing resolution is input for the vertex reconstruction and Monte Carlo simulation.

3.2 Water Transparency

The number of Cherenkov photons observed by a PMT is affected by absorption and scattering in the water. For accurate energy reconstruction, SK has two methods to

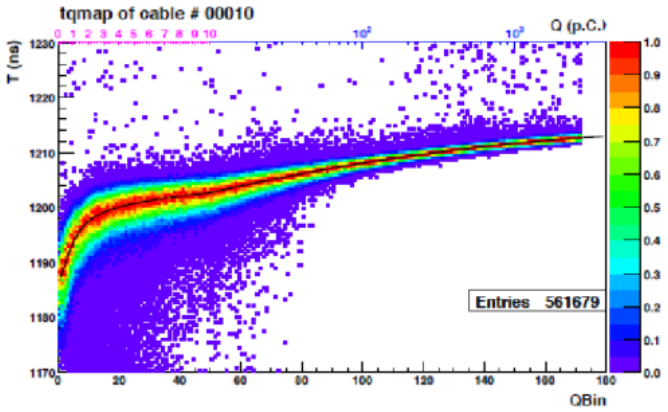

Figure 17: TQ-map, a scatter plot of the PMT timing (vertical axis) and charge (horizontal axis).

measure water transparency, by N_2 laser and decay electrons. The N_2 laser allows the independent measurement of absorption and scattering coefficients. Decay electrons from cosmic ray muons allow the measurement of the effective attenuation length.

3.2.1 Lasers

The wavelength of the lasers are 337, 375, 405, 445, and 473 nm. During normal data taking, the laser is pulsed every 6 sec and injected into the tank vertically from the top by a light injector.

Hits in the bottom PMTs are caused mostly by direct photons, while hits in the barrel and the top PMTs are caused by photons scattered by the water or reflected off the bottom PMTs or the black sheet.

From the total number of scattered photons and the distribution of the arrival-time of PMT hits, the attenuation length parameters are obtained by comparing with the expectations from Monte Carlo simulation. The attenuation length is

$$L_{atten} = \frac{1}{\alpha_{abs} + \alpha_{scat,sym} + \alpha_{scat,asym}}, \tag{10}$$

where $\alpha_{scat,sym}$ is the coefficient of symmetric (i.e. same intensity for forward and backward) scattering, which is mainly due to Rayleigh scattering and Mie scattering, and $\alpha_{scat,asym}$ is the coefficient of asymmetric scattering due to Mie scattering.

These parameters are used for the model of water in the event simulation. The event simulation is consistent with the data of the following decay electron study.

3.2.2 Decay Electrons

There are thousands of muons per day that stop in the tank and decay into electrons. These events can be used as a calibration sample. The following criteria are applied to obtain a pure sample:

- The time difference Δt between the stopping muon and the electron event is $3.0\ \mu sec < \Delta t < 8.0\ \mu sec$.
- The vertex of the electron event is in the fiducial volume.
- The distance between the muon stopping point and the vertex of the electron is less than 250 cm.
- The number of PMT hits in the residual time within 50 ns is larger than 50.

About 700 events/day are selected.

The water transparency is calculated from the distribution of the number of PMT hits versus the distance from the reconstructed vertex to each PMT hit. The PMT hits with opening angle 32° to 52° and the residual time ≤ 50 ns are used for removing noise and indirect hits. The same correction as for the energy reconstruction is applied to the contribution from each PMT. The water transparency for a given day is estimated from the average of the 2 weeks before and after to reduce the statistical fluctuation. Fig. 18 shows the time variation of this water transparency. This value is used as a parameter for the energy reconstruction.

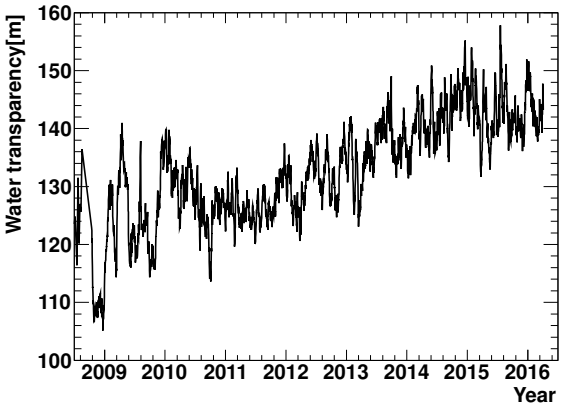

Figure 18: Water transparency of SK-IV measured from decay electron

3.3 Energy Calibration

3.3.1 LINAC

The absolute energy scale is mainly determined from the electron linear accelerator (LINAC) calibration. The LINAC ejects a mono-energetic down-going electron. The beam energy is less than 19 MeV and measured with ±20 keV accuracy by a germanium detector. The details of the LINAC is found in Ref. [23].

The LINAC data was taken in August 2010, July 2012, August 2016, and August 2017. Data were taken at the several ejection heights and electron energies. Various MC parameters are tuned from LINAC data.

The conversion function from the effective hits to the total energy is tuned by LINAC. The function is not directly determined from LINAC data because the events have a fixed vertex and direction. First, fixed energy and uniformly distributed events are generated by the LINAC-tuned MC. Second, the average effective hit (N_{eff}) for each energy is calculated by fitting the N_{eff} distribution with a Gaussian. The relation between energy and N_{eff} is fit with a 4th order polynomial function. This is the function for the absolute energy. The accuracy is better than 1%.

The LINAC data is also used to study the energy resolution, vertex resolution, and angular resolution.

3.3.2 DT generator

The deuterium-tritium (DT) neutron generator is used to cross-check the absolute energy scale. The neutron produces ^{16}N from ^{16}O via (n,p) interactions. ^{16}N has a beta decay Q-value of 10.4 MeV and emits an electron (<4.3 MeV) and γ-ray (6.1 MeV) dominantly. The DT data is measured every few months. The reconstructed energy from DT data matches with the LINAC-tuned MC within ≤1% accuracy. Since DT events are isotropic, the position dependence can be checked. The dependency is less than ± 0.5%. The DT calibration can be done at more radial positions than the LINAC. The radial and height dependency is less than ±0.5% and ±1%, respectively.

3.3.3 Decay Electrons

The spectrum of decay electron events is the well-known Michel spectrum. It can be used to check the energy scale under 60 MeV. Considering the effect of muon capture by oxygen nuclei, the decay electron data is reproduce by MC within ≤2% accuracy.

The time variation of the energy scale is also checked with decay electron data. The 30-days average of N_{eff} is calculated from the same sample as the water transparency measurement. The averaged N_{eff} in SK-IV is shown in Fig. 19. The variation is less than ±1%.

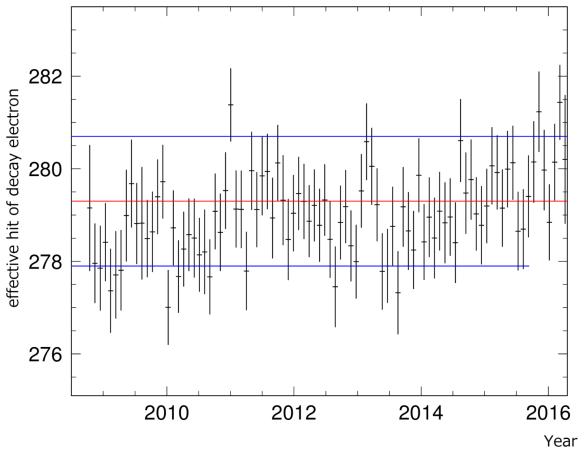

Figure 19: The time variation of the effective hits from decay electrons. It is corrected by water transparency. Red shows the average and the blue shows the $\pm 0.5\%$ line.

4 Event Reconstruction

When an event meets a software trigger condition, that event is reconstructed by a vertex reconstruction tool for low energy events, called "low energy reconstruction tool". After that, event direction and energy are reconstructed. Using the reconstructed vertex, direction, and energy, further reductions are applied to reduce backgrounds.

The muon track fitter is applied to events that have more than 1000 p.e. and meet the HE trigger condition and OD trigger condition. The criterion of more than 1000 p.e. corresponds to muons whose track length is more than about 1 m. The spallation events along a track length of less than 1 m is outside of the fiducial volume and can be removed by the fiducial volume cut. Muon information such as time to low energy event, energy deposit in the detector, and distance from the low energy event and the muon track are used for identify spallation events.

After some reduction process, the Cherenkov angle, the angle between the direction of the charged particle and that of the Cherenkov light, is calculated to identify electron-like events.

4.1 Vertex Reconstruction

The vertices of low energy events are reconstructed only from the PMT hit timing, because most of the PMT hits are caused by a single photon. Due to the short travel distance of low energy electrons and positron ($\sim$20 cm at 50 MeV), Cherenkov light is considered as emitted from a point source. The fitter BONSAI (Branch Optimization Navigating Successive Annealing Iterations) works as follows [48].

BONSAI fits the maximum likelihood function of the timing residual of the hit PMTs. For a test vertex ($\vec{v}$) and a test event start time (t_0), the timing residual is defined as:

$$\Delta t_i = t_i - \mathrm{tof}(\vec{v}) - t_0, \tag{11}$$

where t_i is timing of a PMT hit and $\mathrm{tof}(\vec{v})$ is the time-of-flight from the test vertex to the hit PMT. The likelihood is calculated from the probability density function of Δt_i as

$$Likelihood = \sum_{i=1}^{N_{hit}} log(P(\Delta t_i)). \tag{12}$$

The $P(\Delta t_i)$ is obtained from the LINAC calibration. For a LINAC event, the vertex and the event start time is known. We can get true Δt distribution. Fig. 20 is this distribution normalized as the peak height = 1 and it is used as $P(\Delta t_i)$. The two peaks after the main peak are caused by re-incidence of electrons reflected by the dynodes. Since Δt_i for the true vertex and start timing distributes like Fig. 20,

the point with maximum likelihood is selected as the vertex. The goodness of the fitting is also calculated. The vertex resolution of BONSAI fit is 70 cm for 10 MeV electrons.

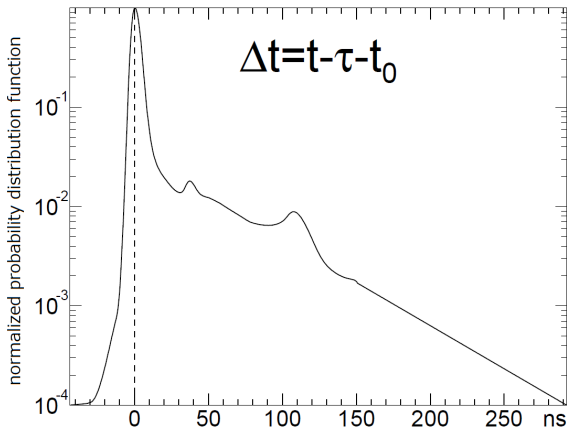

Figure 20: Probability distribution of TOF normalized as the peak height = 1.

4.2 Direction Reconstruction

The direction of the charged particle is reconstructed from the Cherenkov ring pattern. The $\vec{d}$ which maximize the following likelihood function L is the event direction,

$$\mathrm{L}(\vec{d}) = \sum_{i}^{N_{20}} log(f(\cos\theta_{dir,E})_i) \times \frac{\cos\theta_i}{a(\theta_i)}, \tag{13}$$

where N_{20} is the number of hit PMTs in a 20 nsec window, $f(cos\theta_{dir,E})$ is the expected distribution of the opening angle, and $\theta_{dir,E}$ is the angle between $\vec{d}$ and the vector from the vertex to a PMT($\vec{d'}$). $\cos\theta_i/\mathrm{a}(\theta_i)$ corrects the PMT acceptance, where θ_i is the opening angle between $\vec{d'}$ and the vector normal to the PMT surface.

The resolution of the direction reconstruction is 25° for 10 MeV electrons.

4.3 Energy Reconstruction

The number of Cherenkov photons is approximately proportional to the energy deposit by a charged particle. For low energy events, the number of hit PMTs is also proportional to the energy deposit, because most of the PMT hits are caused by a

single photon. The energy reconstruction method is based on this idea with some corrections added. The hits of its residual time in 50 ns window is the target. This narrow window removes most of the dark noise. From N_{50} PMT hits, the effective hits (N_{eff}) is calculated as:

$$N_{eff} = \sum_{i}^{N_{50}} (X_i - \epsilon_{tail} - \epsilon_{dark}) \times \frac{N_{all}}{N_{norm}} \times \frac{R_{cover}}{S(\theta_i, \phi_i)} \times exp\left(\frac{r_i}{\lambda(run)}\right) \times G_i(t), \quad (14)$$

where:

- Occupancy X_i
  The occupancy X_i is the correction for multiple photo-electrons from a relatively high energy event. When a PMT has multiple p.e., the other PMTs around that PMT tend to have a hit. The occupancy X_i is defined as a function of the ratio (x_i) of hit PMTs to all PMTs around the PMT:

$$X_i = \begin{cases} \frac{log\frac{1}{1-x_i}}{x_i} & x_i < 1 \\ 3.0 & x_i = 1 \end{cases} \quad (15)$$

- Late hits ϵ_{tail}
  Some photons are outside the 50 ns window due to scattering or reflection. ϵ_{tail} corrects this effect.

- Dark Noise ϵ_{dark}
  ϵ_{dark} is the correction to remove hits by dark noise. The value is calculated from the number of operating PMTs and the dark noise rate.

- Bad PMTs N_{all}/N_{norm}
  This term corrects the number of PMTs. N_{all} is the number of all PMTs. In SK-IV, N_{all} is 11,129. N_{norm} is the number of operating PMTs.

- Photo-cathode coverage $R_{cover}/S(\theta_i, \phi_i)$
  The PMT coverage R_{cover} is corrected by $S(\theta_i, \phi_i)$, the coverage depending on the incident angle. The incident angle is calculated from the reconstructed vertex.

- Water transparency λ
  The attenuation in the water is corrected by the observed water transparency λ and the distance r_i between the vertex and the PMT.

- PMT gain $G_i(t)$
  $G_i(t)$ is the gain for a single photon depending on time.

The total energy is reconstructed as a function of N_{eff}. The function is calibrated with LINAC data (Sec. 3.3.1). The uncertainty in the absolute energy scale is better than 1%. The energy resolution is 14% for 10 MeV electrons.

This energy reconstruction is for an electron or positron.

4.4 Muon Reconstruction

Most of the events that remain after the fiducial volume cut in the energy range between 6 MeV and 20 MeV are spallation products by cosmic ray muons. The spallation events can be removed by searching for spatial and timing correlation with preceding muons. Therefore, the precise reconstruction of muon events is important.

4.4.1 Muboy Fitter

Events with more than 1000 p.e. are fitted by a fitter, Muboy [55, 46]. Muboy fits a single track muon and multiple ($\leq$10) track muons. The fitted muon event is classified as a single through-going muon, a stopping muon, multiple muons, or a corner clipper. When an event is fitted as multiple muons and its second track has a few hits after removing the hits of the first track, the event is classified as one track multiple muons. Muboy also returns a goodness value of the fit quality.

Due to the wide time window at SK-IV, a muon can be accidentally included in the window of another event and not tagged as a muon event. There are a few hundreds of untagged muons per day. To search for untagged muons and remove spallation events from them, the software trigger is applied to each event. Muboy is applied to these extracted untagged muons.

4.4.2 Brute Force Fitter

The Brute Force Fitter (BFF) is another fitter for the single through-going muons poorly fitted by Muboy. If the Muboy goodness is less than 0.4, the BFF is applied. BFF searches for the muon entry and exit point in a grid on the inner surface of the detector [34]. It takes more time than Muboy. BFF correctly fits 75% of badly fit muons by Muboy and improves spallation cuts.

4.4.3 Energy Loss

The muon energy loss along the track tends to be maximum at the point where the muon causes spallation. After fitting the muon track, the energy loss per unit length along the track, dE/dx, is calculated. From timing information, the light each PMT catches and the point on the track is matched.

4.5 Cherenkov Angle Reconstruction

In the low energy analysis, particles can be identified mainly by Cherenkov opening angle. The electron and positron are ultra-relativistic and exhibit a Cherenkov angle of about 42°. Heavier particles such as muons or pions are not ultra-relativistic and have smaller Cherenkov angle. PMT hits by multiple γ-rays are isotropic and not shaped as a clear ring.

The Cherenkov angle is reconstructed from a 3-hit combination. Every combination of 3 PMTs gives an opening angle. The distribution of opening angles for all combinations of hit PMTs have a peak at the Cherenkov angle of the event. To reduce the effect of PMT dark noise, only the PMT hits whose residual time is in the 15 ns window are used. Here, those 3 PMTs are viewed from the reconstructed vertex position. A typical electron event is shown in Fig. 4.5. In the left panel, the Cherenkov angle is fitted at 43.2°. Since the shape of the distribution is difficult to parameterize, a sliding window in which the contents of neighboring 7 bins are added to the middle bin is used for searching for the peak instead of fitting.

A typical muon event is shown in Fig. 4.5. It has a different opening angle distribution. The Cherenkov angle is fitted at 31.5°.

A typical γ-ray event is shown in Fig. 4.5. The distribution is isotropic and fitted at 87.3°.

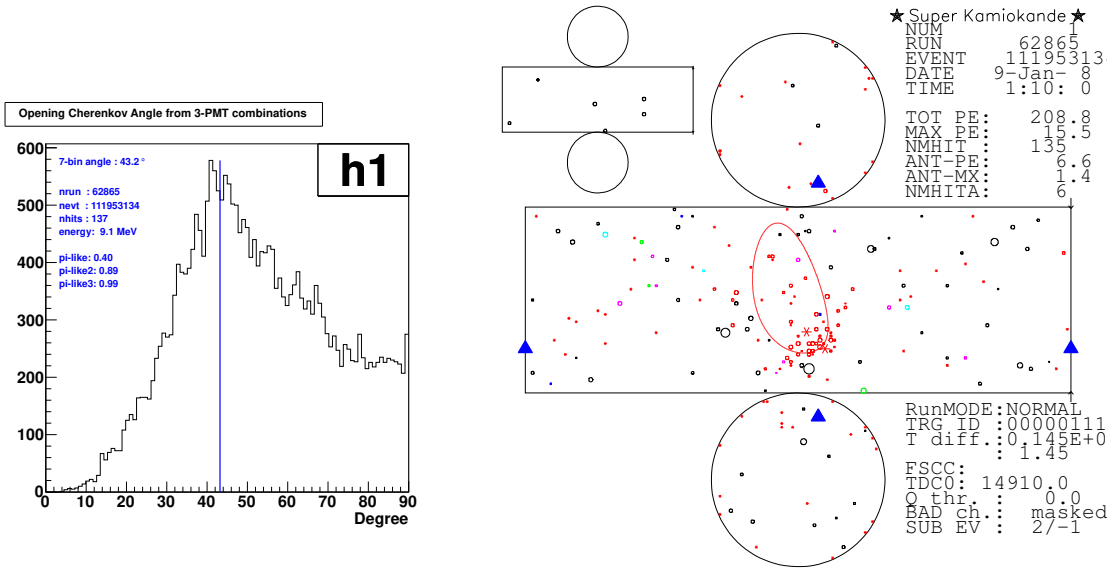

Figure 21: Typical electron event. Left: opening angle distribution, right: event display.

A typical relatively high energy pion event is shown in Fig. 4.5. The reconstructed Cherenkov angle is 44.1°. This kind of event cannot be distinguished be from electron

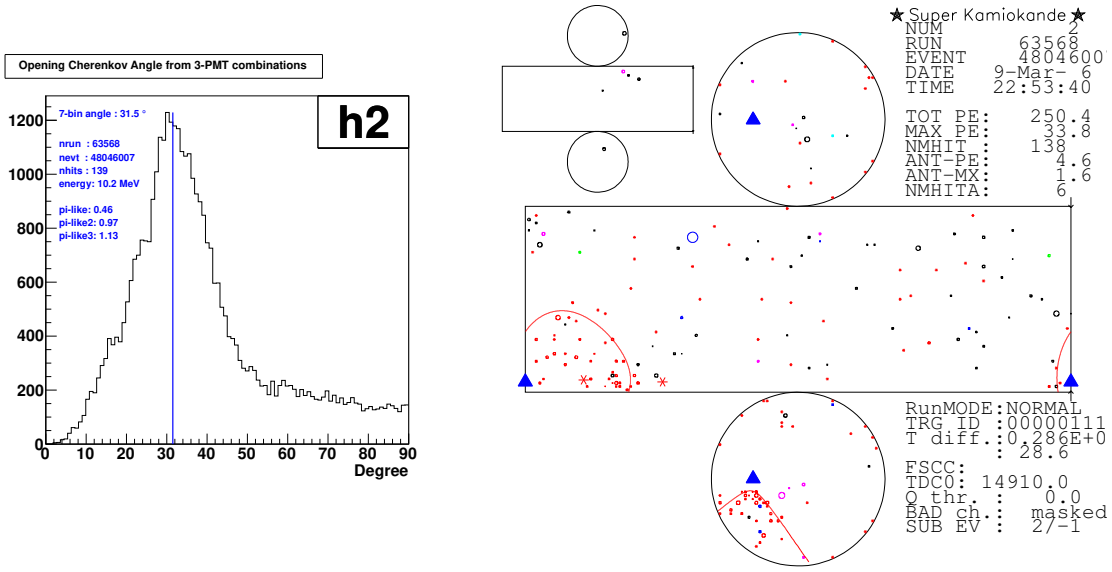

Figure 22: Typical muon event. Left: opening angle distribution, Right: event display.

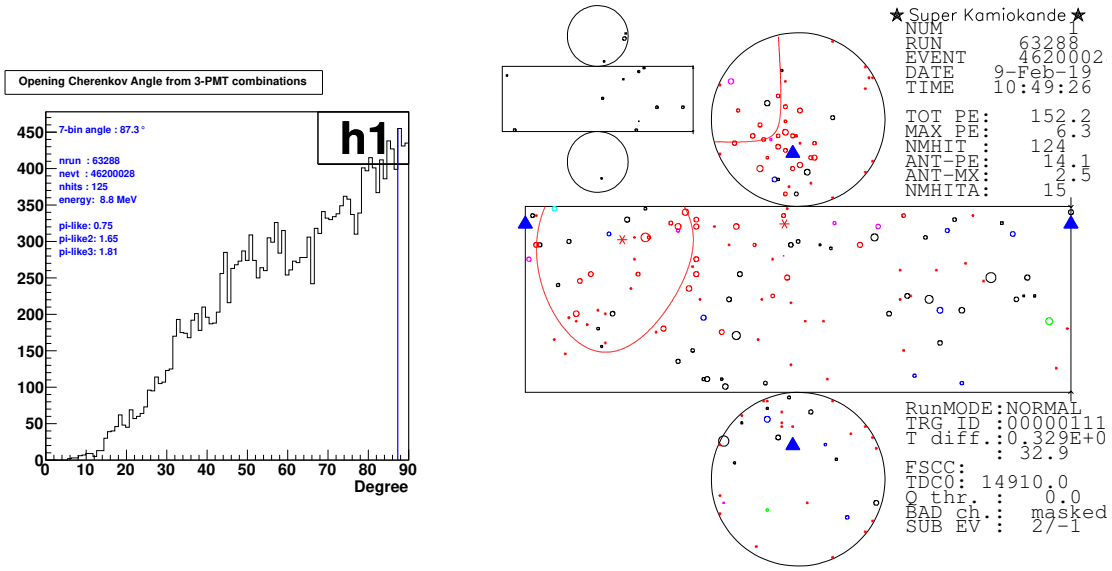

Figure 23: Typical γ-ray event. Left: opening angle distribution, Right: event display.

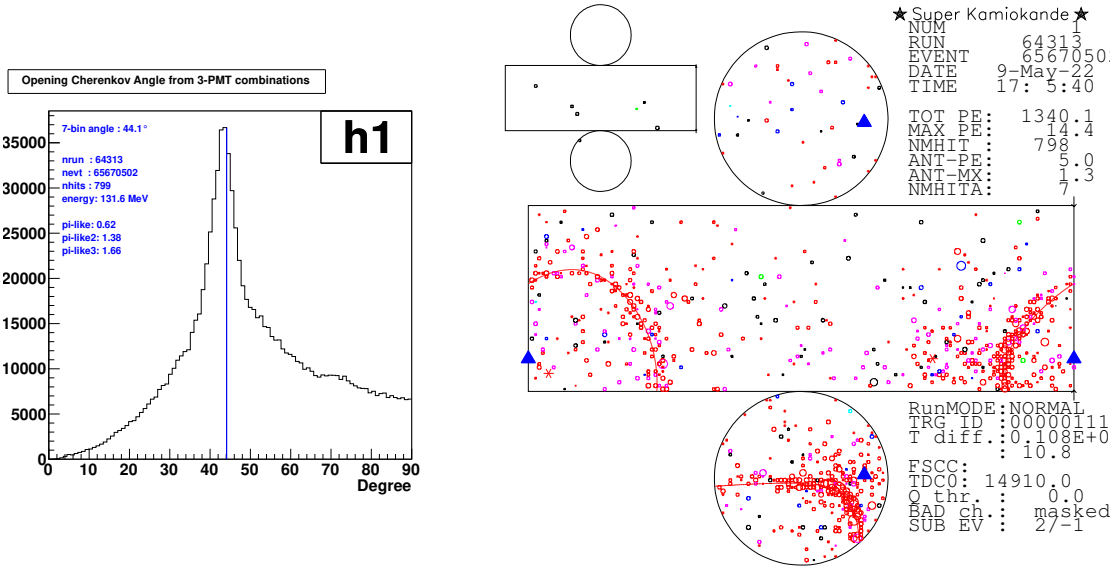

Figure 24: Typical pion event. Left: opening angle distribution, Right: event display.

events by Cherenkov angle. Therefore, the peak width is used. The ring of a pion event is sharp while the ring of an electron event is fuzzy. The ring sharpness is related to the peak width of the opening angle distribution. The peak width is evaluated with a pion likelihood:

$$\pi_{\text{like}} = \frac{\text{number of PMT sets in } \pm 3^\circ \text{ around peak}}{(\text{number of PMT sets in } \pm 10^\circ \text{ around peak}) - (\text{number of PMT sets in } \pm 3^\circ \text{ around peak})}. \quad (16)$$

5 Event Simulation

To evaluate the reduction efficiency, a Monte Carlo simulation sample is used.

5.1 Detector Simulation

The Super-Kamiokande detector simulation package, SKDETSIM, is based on GEANT 3.21. SKDETSIM include three steps in the simulation as follows,

- Tracking of particles in the water.
- Propagation of emitted Cherenkov photons in the water.
- Detection of Cherenkov photons by PMTs and electronics.

The generated photons are attenuated in water and reflected by the detector structure and impurities in water. The photo-electron generated at a PMT surface is recorded according to the timing resolution of PMTs. These parameters are tuned to reproduce the calibration data[40, 39].

5.1.1 Particle Tracking

For particle tracking, GEANT 3.21[2] is used. It is a system developed at CERN to simulate electromagnetic processes. In addition to Cherenkov radiation, multiple scattering, ionization, δ-ray production, Bremsstrahlung, and e^+ annihilation are considered for electrons. For gamma-rays, e^+e^- pair creation, Compton scattering, and the photo-electric effect are taken into account.

The direction of Cherenkov photon emission is calculated as $\cos\theta = 1/n\beta$. The refractive index n depends on the wavelength, the water temperature and pressure. The number of emitted photons along the trajectory of a charged particle per wavelength is calculated as Eq. 5.

5.1.2 Cherenkov Photon Tracking

The emitted photons propagate and are scattered and absorbed by water molecules. The group velocity v_g of light in water is defined as

$$v_g = \frac{c}{n(\lambda) - \lambda\frac{dn(\lambda)}{d\lambda}}, \tag{17}$$

where c is the speed of light in vacuum, λ is the wavelength of the photon, and $n(\lambda)$ is the effective refractive index.

The considered photon interactions are Rayleigh scattering, Mie scattering, and absorption. Due to the shorter wavelength of Cherenkov photons compared to the radius of water molecules, Rayleigh scattering is dominant. Rayleigh scattering has

a $1/\lambda^4$ dependence in the short wavelength region. The effect of absorption becomes larger for the longer wavelength. The dependence is studied in [14].

The coefficients of water quality are tuned with the LINAC calibration at some wavelength (See Sec. 3.3.1). The time dependence of the water quality is monitored by the N_2 laser calibration and decay electrons.

5.1.3 Photon Detection by PMT and Electronics

After a photon reaches a PMT surface, the responses of the PMT and electronics are calculated.

- Whether a photo-electron can be emitted or not
  is determined from the quantum efficiency of the PMT (Fig. 9).
- The output charge
  is simulated from the charge distribution of a single photo-electron (Fig. 25).
- The PMT hit timing
  is calculated considering the timing resolution of the PMTs as a Gaussian random variable with a 1σ width (Fig. 26).
- The dark noise
  are determined as randomly distributing throughout the detector with the measured dark noise rate.

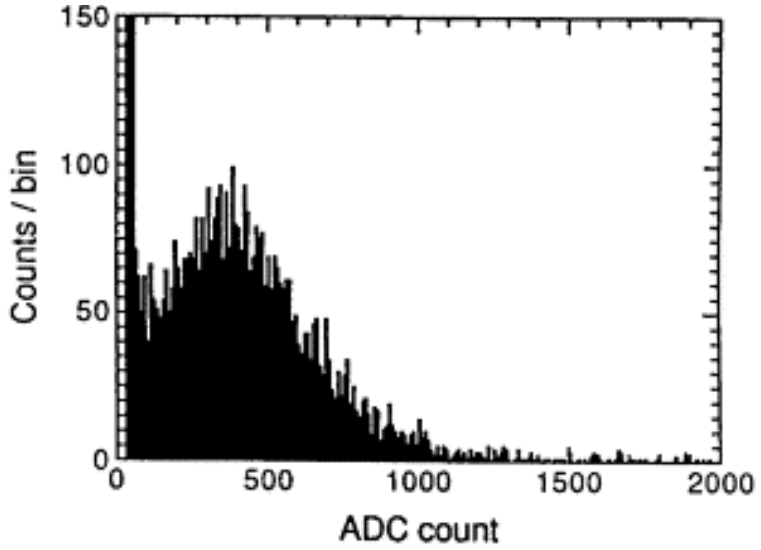

Figure 25: Single photo-electron pulse height distribution. The peak close to 0 ADC count is due to PMT dark current. From [25].

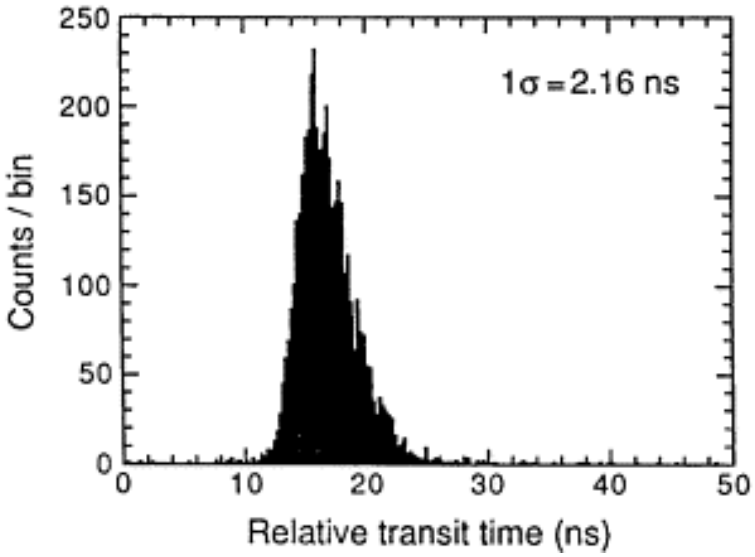

Figure 26: Relative transit time distribution for a typical test with 410 nm wavelength light at the single photo-electron intensity level. From [25].

5.1.4 Water Transparency

The attenuation in water is related to the propagation of Cherenkov photons. The intensity reduces exponentially:

$$I(x) = I_0(\lambda) exp(-x/L(\lambda)), \tag{18}$$

where I_0 is the initial intensity, x is the traveling length and L is the total attenuation length (water transparency). The water transparency consists of 3 coefficients, absorption α_{abs}, Rayleigh scattering α_{Ray}, and Mie scattering α_{Mie}. The angular distribution of Rayleigh scattering is symmetric. Mie scattering favors the forward direction. The empirical equations for the water transparency are:

$$\begin{aligned} L_{MC}(\lambda) &= \frac{1}{\alpha_{abs} + \alpha_{sym} + \alpha_{asym}} \\ \alpha_{abs} &= P_0 \times \frac{P_1}{\lambda^4} + C \\ \alpha_{sym} &= \frac{P_4}{\lambda^4} \times (1.0 + \frac{P_5}{\lambda^2}) \\ \alpha_{asym} &= P_6 \times (1.0 + \frac{P_7}{\lambda^4} \times (\lambda - P_8)^2, \end{aligned} \tag{19}$$

where $P_{1\ 8}$ are fitting parameters. The parameters are tuned with calibration data.

The water transparency has position dependency due to the convection under z = -11 m. It is monitored by two calibration sources, auto Xenon light and Ni-Cf. The hit rate of the top PMTs and the bottom PMTs is used. The difference, top-bottom asymmetry (TBA), is defined as:

$$TBA = \frac{< top > - < bottom >}{< barrel >}, \tag{20}$$

where $< top >$ is the mean hit rate for the top PMTs and so on. The absorption coefficient is corrected with TBA:

$$\begin{aligned} \alpha_{abs}(\lambda, z) &= \alpha_{abs}(\lambda) \times (1.0 + \beta z), z \geq -11\ m \\ &= \alpha_{abs}(\lambda) \times (1.0 - 1100\beta) z < -11\ m. \end{aligned} \tag{21}$$

5.2 Neutrino Interaction Simulation

Inverse beta decay has been studied theoretically. In this thesis, Strumia and Vissani's calculation[49] is used for the cross-section of $\bar{\nu_e} p \rightarrow e^+ n$. The energy of the positron is approximated as:

$$\begin{aligned} E_e &= E_\nu - \Delta \\ \Delta &= M_n - M_p \approx 1.293\ MeV. \end{aligned} \tag{22}$$

To get the reduction efficiency, the electron event is generated as follows:

- Set electron energy, mono energetic (above 24 MeV) or randomly in the target range (below 24 MeV).
- Set electron vertex in the SK full volume and direction randomly.
- Attach time information to consider water transparency.
- Simulate the detector reaction for the generated events by SKDETSIM.

6 Data Reduction for GRB Neutrino Search

6.1 Data Set

The neutrino search was done for SK-IV data. At the beginning of SK-IV, GPS information was not available. Therefore, the target period is from December 7, 2008 to May 31, 2017.

The GRB database is based on the Gamma-Ray Candidate Network (GCN). The GCN distributes two types of information, the notices and circulars. A notice gives the GRB location detected by the satellites. Most of the notices distribute during the burst to the follow-up observations. A circular contains the various data of follow-up observations by optical, radio, X-ray, TeV photons, or other particles.

Because circulars are unformatted e-mail messages, the system extracting information from the GCN circulars was developed. The database by the system, grbweb online catalog[1], parses all GRBs archived at GCN circulars once a day. In the grbweb, parameters like GRB time, direction, start time, stop time, and redshift are included. When different values are reported from different satellites, one value is selected by a fixed order. The lists of that order and of parameters each satellites gives are shown in Ref. [7].

2208 GRB were observed during SK normal data taking.

6.2 First Reduction

By first reduction, non-physical events and background events that are obviously decay electron events or events near the wall are removed. This reduction is based on that of the solar neutrino analysis and supernova relic neutrino search.

6.2.1 Calibration Event Cut

During normal data taking, calibration by laser and Xe light is done periodically. The calibration events are marked by a specific event flag and ID trigger. We use the events without these flags.

6.2.2 Noise Event Cut

One PMT flashes a thousand times per second. This sometimes causes noise events. The p.e. by dark noise tend to be little, therefore the ratio of charge which is less than 0.5 p.e. to total charge is used for the noise event cut. Fig. 27 shows the distribution of this ratio. Events with more than 0.55 ratio are removed.

[1] http://grbweb.icecube.wisc.edu

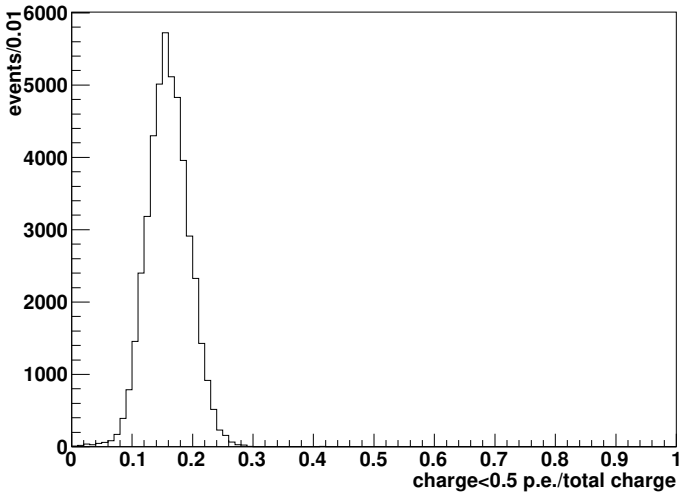

Figure 27: ratio of charge < 0.5 p.e. to total charge

6.2.3 OD cut

OD triggered events are the ones where charged particles come from outside of the detector. We remove these events.

6.2.4 50 μs Time Difference Cut

Events after the 50μs LE trigger events or after un-tagged muon events are removed. Un-tagged muon events are events included in the preceding HE trigger. A software trigger requiring HE and OD trigger pair is applied to the events in a 35 μs window after HE trigger. The events removed by this cut may be decay electron events or ringing noise events from cosmic ray muons. The cosmic ray muons come into the detector at 2 Hz. Fig. 28 shows the distribution of the time difference from the last LE trigger to the events after Sec. 6.2.1-Sec. 6.2.3 reductions. It has a peak at 0 nsec caused by decay electron events and ringing noise and tail after $\sim$50 nsec caused by independent muons.

6.2.5 Fiducial Volume Cut

The SK detector is surrounded by rock. The radioactive events from the rock are detected near the SK wall. The events with vertex within 2 m from wall are removed.

The fiducial volume cut is applied in two stages. At first, the events within 1 m

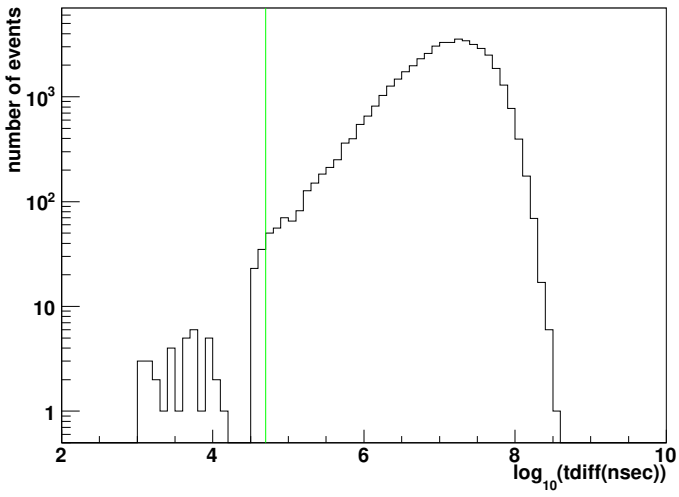

Figure 28: Time difference from the last LE trigger to an event.

from the wall are removed. The vertex distribution before the cut is shown in Fig. 29. After this rough fiducial volume cut, the candidate events of the spallation parent muon are selected. The parent muon for the spallation events in the fiducial volume is less likely to be missed at muon selection.

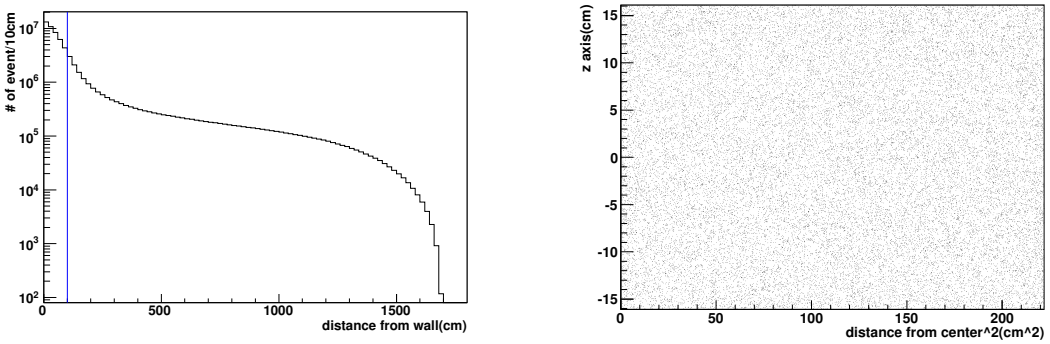

Figure 29: Vertex distribution at first reduction. Left: histogram of distance from the wall. Right: scatter plot of z versus $x^2 + y^2$.

6.2.6 Goodness Cut

We select well reconstructed events by a goodness cut. The combination of two goodnesses G_v and DirKS is used. G_v shows the quality of vertex reconstruction and DirKS the uniformity of azimuthal angle. The combined variable ovaQ (One dimensional variable of Vertex and Angular reconstruction Quality) is defined as $G_v^2 - \mathrm{DirKS}^2$. As shown in Fig. 30, the ovaQ distribution has two peaks, one at $\sim$0 from badly reconstructed events and the other at $\sim$0.4 with well reconstructed events. When ovaQ is less than 0.2, the event is removed.

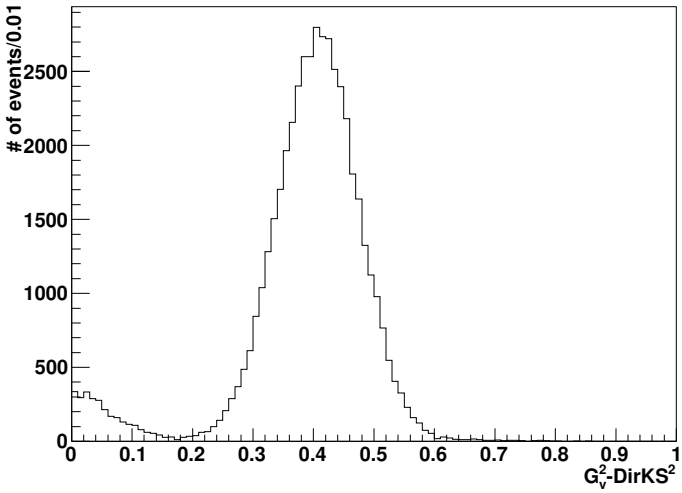

Figure 30: Distribution of ovaQ, $G_v^2 - \mathrm{DirKS}^2$.

6.3 Spallation Cuts

Cosmic ray muons induce radioactive nuclei when muons produce hadronic cascade showers in the detector. To remove the event from the decay of this radioactive isotope, following reduction was applied.

The spallation cuts are tuned for the supernova relic neutrino study [54]. The possible radioactive isotopes induced by cosmic ray muons are listed in Table 1.

The spallation cuts are based on four variables, Dt, lt, ln, and Q_{peak}, where

- Dt, time difference to a muon event.
- lt, transverse distance from muon track.

Table 1: The possible radioactive isotopes induced by cosmic ray muons.

Isotope	Mean-life(s)	Decay mode	$E_{kin.}$(MeV)	Primary process
$^{11}_{4}$Be	19.9	β^-	11.51	(n, α+2p)
		$\beta^-\gamma$	9.41+2.1(γ)	
$^{16}_{7}$N	10.3	β^-	10.44	(n,p)
		$\beta^-\gamma$	4.27+6.13(γ)	
$^{15}_{6}$C	3.53	β^-	9.77	(n,2p)
		$\beta^-\gamma$	4.51+5.30(γ)	
$^{9}_{3}$Li	1.21	β^-	$\sim$13.0	$(\pi^-, \alpha + {}^2\mathrm{H} + p + n)$
$^{8}_{5}$B	1.11	β^+	$\sim$13.9	$(\pi^+, \alpha + 2p + 2n)$
$^{16}_{6}$C	1.08	$\beta^- + n$	$\sim$4	$(pi^-, n + p)$
$^{9}_{3}$Li	0.26	β^-	13.6	$(pi^-, \alpha + 2p + n)$
		$\beta^- + n$	$sim10$	
$^{9}_{6}$C	0.18	$\beta^+ + p$	3$\sim$15	$(n, \alpha + 4n)$
$^{8}_{2}$He	0.17	$\beta^-\gamma$	9.67+0.98(γ)	$(\pi^-, {}^3\mathrm{H} + 4p + n)$
		$\beta^- + n$		
$^{12}_{4}$Be	0.034	β^-	11.71	$(\pi^-, \alpha + p + n)$
$^{12}_{5}$B	0.029	β^-	13.37	$(n, \alpha + p)$
$^{13}_{5}$B	0.025	β^-	13.44	$(\pi^-, 2p + n)$
$^{14}_{5}$B	0.02	$\beta^-\gamma$	14.55+6.09(γ)	(n,3p)
$^{12}_{7}$N	0.016	β^+	16.38	$(\pi^+, 2p + 2n)$
$^{13}_{8}$O	0.013	$\beta^+ + p$	8$\sim$14	$(\mu^-, \mu^- + p + 2n + \pi^-)$
$^{11}_{3}$Li	0.012	β^-	20.62	$(pi^+, 5p + \pi^0 + \pi^+)$
		$\beta^- + n$	$\sim$16	

- Q_{peak}, the maximum value of energy deposit of the muon, dE/dx for 50 cm bin along muon track.
- ln, longitudinal distance from the spallation point where dE/dx is maximum.

These variables are calculated for the muons within 30 sec before the low energy event (Fig. 31-Fig. 34). Cosmic ray muons are categorized into four types, single through-going muon, multiple muons, stopping muons, and corner-clipping muons. The cut for stopping muons was applied at a later stage (N16 cut). To get the cut efficiency, a random sample is prepared. In the random sample, muons 30 sec or less after low energy event are selected. The efficiency is shown in Table 2.

Table 2: Efficiency for the spallation cut.

Energy (MeV)	Efficiency
9.0	83.2%
10.5	85.6%
11.5	85.5%
13.0	85.2%
15.0	83.5%
21.0	92.5%
27.0	100%

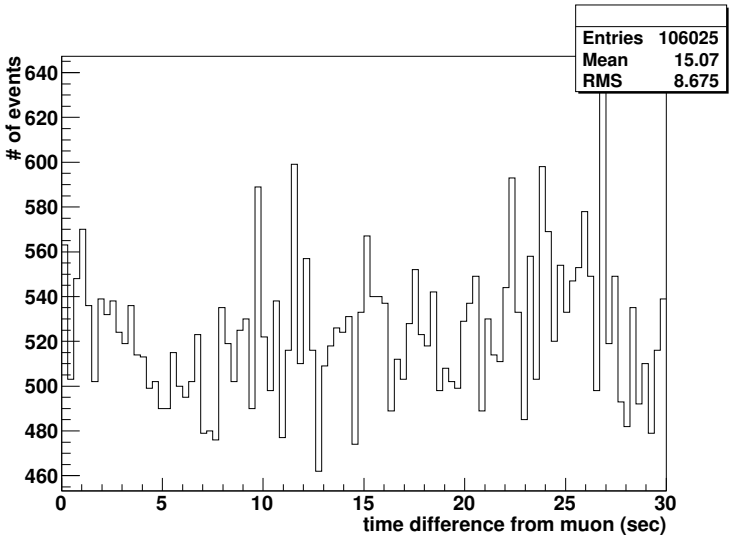

Figure 31: Time difference from a muon.

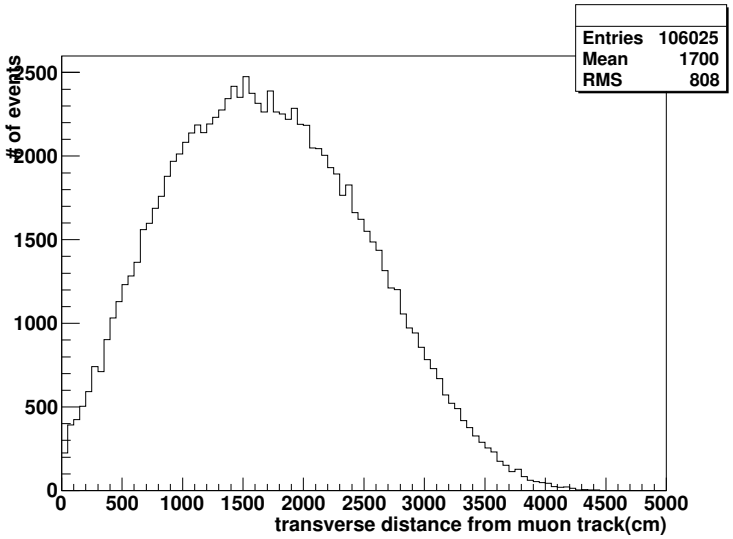

Figure 32: Transverse distance from the muon track.

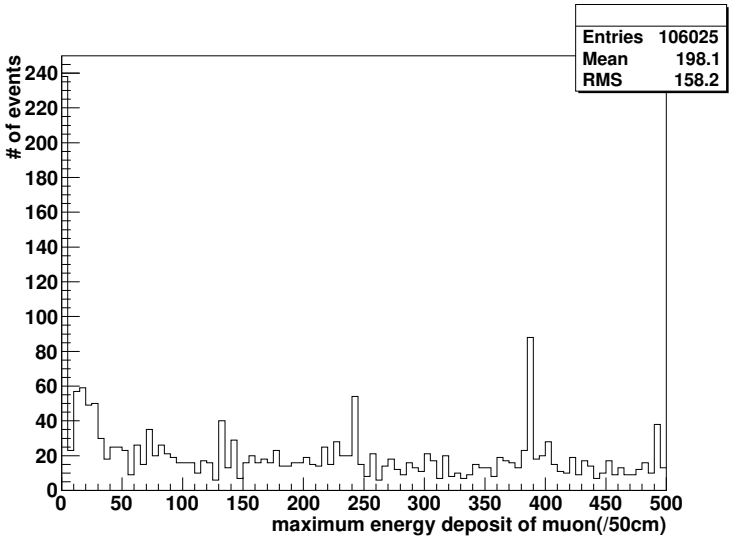

Figure 33: Maximum energy deposit of the muon along its track.

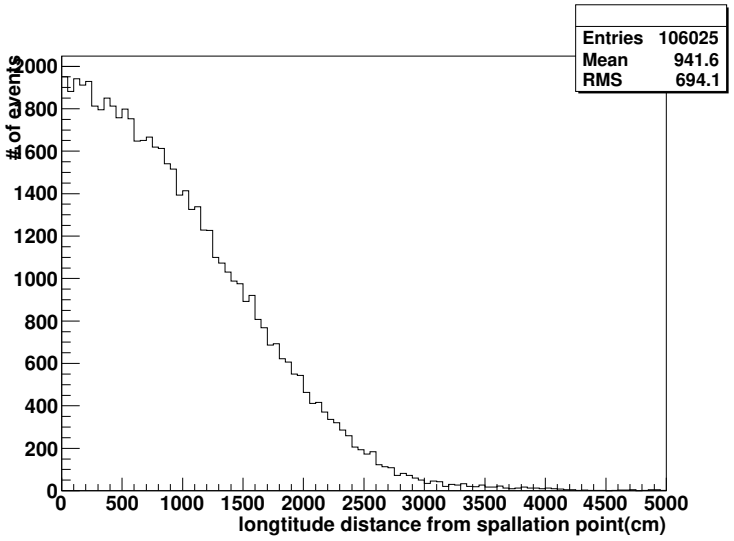

Figure 34: Longtitudinal distance from the spallation point to the maximum energy deposit point.

6.4 Gamma cut

The events incoming from outside the detector, such as environmental gamma-rays from the surrounding rock are removed. For this cut, the variable effwall is used. As shown in Fig. 35, effwall is the expected travel distance from the ID wall. It is calculated from the vertex position and the event direction. The threshold is effwall 300 cm above 22 MeV and 450 cm under 22 MeV (Fig. 36).

6.5 Pion Cut

Atmospheric neutrinos sometimes make pions in the detector. The pion events with higher momentum have a similar Cherenkov angle compared to neutrino events. The pions soon interact in the water, lose energy, and stop emitting Cherenkov light. Their rings are sharper than the neutrino ones. π_{like} defined as:

$$\pi_{\rm like} = \frac{\text{number of entry in } \pm 3^\circ\text{from peak}}{\text{number of entry in } \pm 10^\circ \text{ from peak} - \text{number of entry in } \pm 3^\circ \text{ from peak}}, \tag{23}$$

which shows the sharpness of the ring. The distribution of π_{like} (Fig. 37) has a peak from electron evens at $\sim$0.4 and a tail depending on the length of a π emitting Cherenkov light. The events with $\pi_{like} >= 0.58$ are removed. Fig. 38 shows an event display of a e-like and π-like event. The e-like event has ambiguous ring pattern and its π_{like} is 0.34. The π-like event has sharp ring patter and its π_{like} is 1.47.

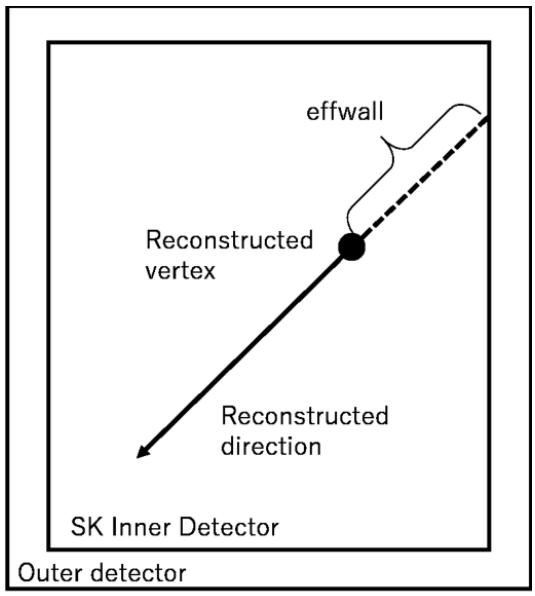

Figure 35: Definition of effwall.

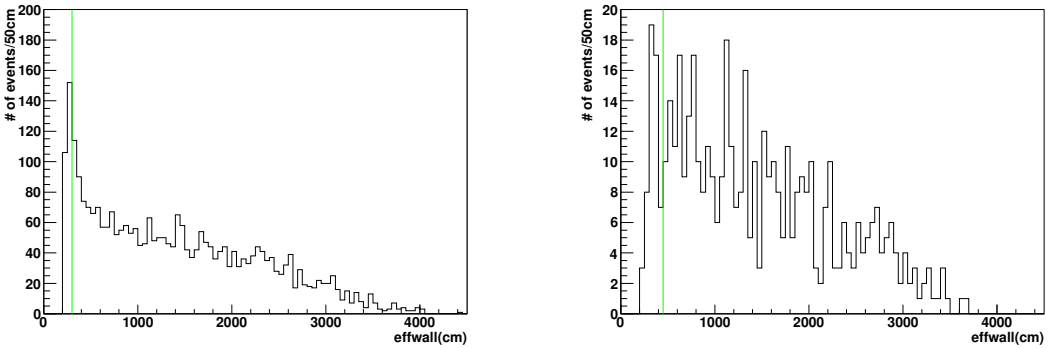

Figure 36: Distribution of effwall. Left: under 22 MeV, right: above 22 MeV.

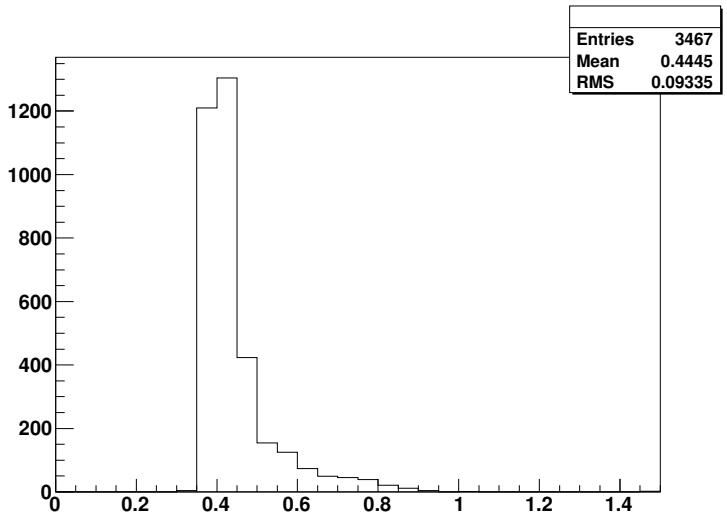

Figure 37: The distribution of π_{like}.

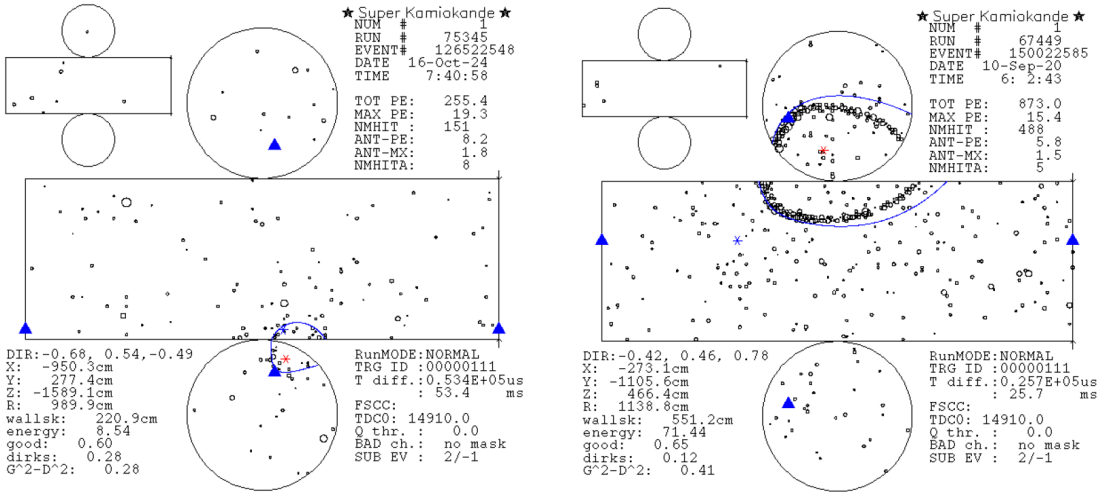

Figure 38: Event display of an e-like event (left) and π-like event (right).

6.6 OD Correlated Event Cut

Because the OD coverage is lower than the ID, some incoming events are not triggered as an OD event. To remove these events, the correlation of ID and OD is searched.

First, the peak of ID hits in a 50 ns sliding time window is searched considering the time of flight from the candidate vertex. Then, OD hits within 5 m from the candidate vertex and 150 ns from the ID peak is counted. The events with 2 or more OD hits are removed. A schematic view of such an event is shown in Fig. 39.

In addition, the peak of OD hits in a 100 ns sliding time window is searched within 5 m from the candidate vertex. The events with 3 or more OD hits are removed.

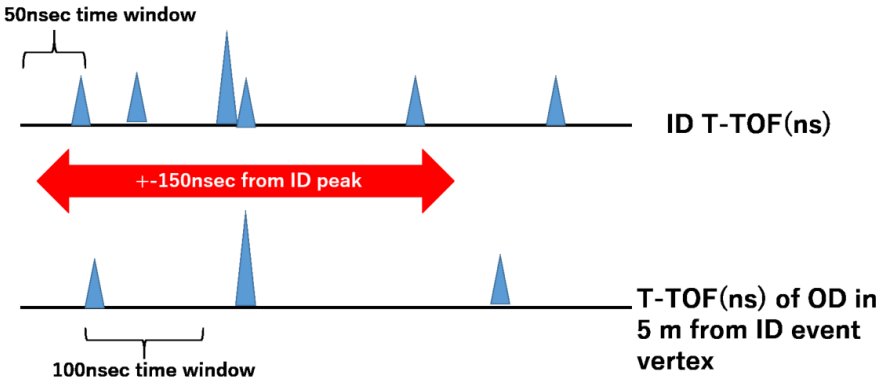

Figure 39: Schematic view of the OD correlated event cut.

6.7 Multi-Ring Cut

The events that have two rings and an angle between rings more than 60° are removed. This cut removes atmospheric neutrino events that have a charged lepton and a charged pion in the same event. They can produce multiple charged particles. Since the ring pattern of a single electron event is fuzzy, it sometimes looks like multiple rings.

A ring pattern fit is performed with a tool from Ref. [41]. After reconstruction of the vertex position and dominant ring by the vertex fitter, the ring fitter looks for a second ring by a pattern recognition technique using a Hough transformation [12]. The ring fitter repeats this four times (5th ring) while a probable ring can be found. The fitter returns the number of rings and the direction of each ring.

To save these single electron events, only the multiple ring events with an angle between rings more than 60° are removed. The distribution of angles between two rings is Fig. 6.7. The threshold, 60° is between peaks at $\sim 40°$ and $\sim 90°$.

Fig. 6.7 shows a typical multi ring event. The PMT hit timing after time-of-flight subtraction looks like one event, but two rings are clearly seen in the event display. The fitted angle for this event is 104°.

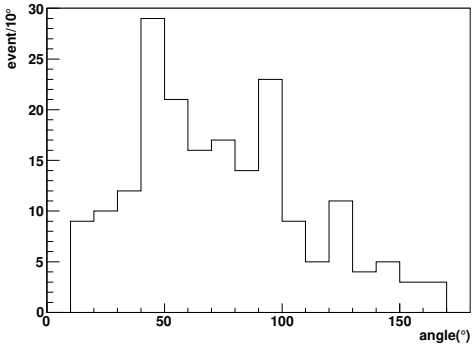

Figure 40: Angle between 2 rings.

6.8 Solar Events Cut

Events like solar neutrinos are removed. Since they interact via $\nu + e^- \rightarrow \nu + e^-$, the direction of the scattered electrons are oriented in the direction from the sun to the earth to some extent.

Total energy, multiple scattering goodness (MSG), and angle to the sun are used. MSG shows the goodness of anisotropy of the PMT hit pattern[4]. During Cherenkov light emission, electrons scatter multiple times. The multiple scattering makes the ring pattern broader and the angular resolution worse. MSG is calculated as follows:

- Select pairs of hit PMTs within 20 ns from the initial event time after TOF subtraction. The vectors from the vertex to each PMT are defined as "hit direction"'s.
- From the vertex, cones with 42° opening angle to the hit directions are projected. For each pair of hit PMTs, 2 cones intersect at 0, and 1 or 2 points on the detector surface.
- When pairs of PMT have 2 intersection points, the unit vector from the vertex to the 2 intersections are taken. All the possible pairs of hit PMTs, this "unit vector" are found.
- For each candidate of "unit vector", the "sum vector" is defined as a vector sum of the "unit vectors" in 50° of that "unit vector". The longest "sum vector" is selected as the "best direction vector" and its direction as the "best direction".

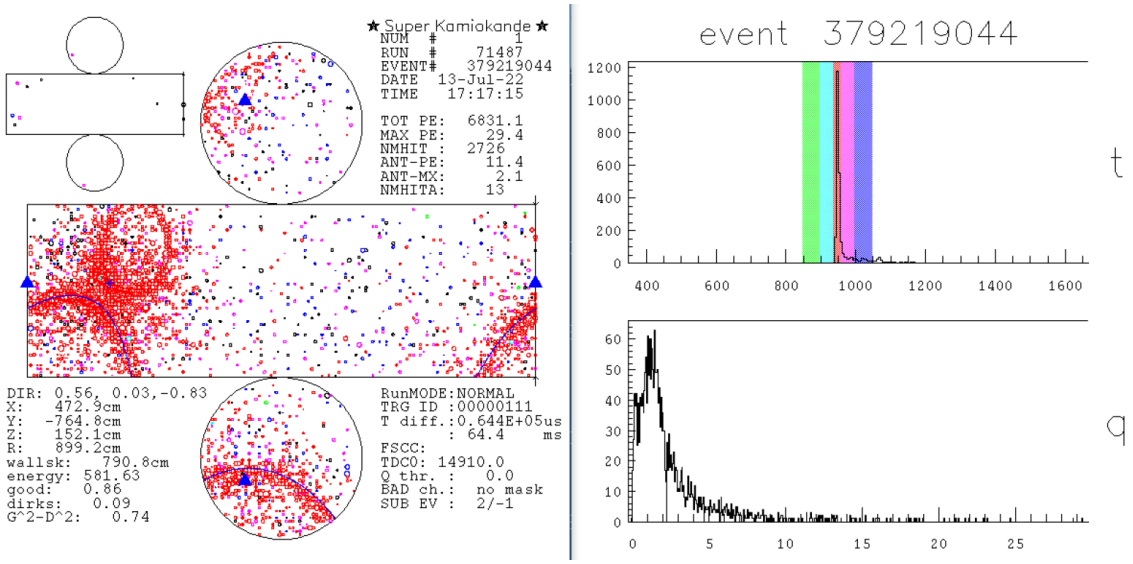

Figure 41: Typical multi-ring event. The left is the event display. The top-right is the PMT hit timing distribution after time-of-flight subtraction. The bottom right is the charge distribution.

- The MSG value is

$$\text{MSG} = \frac{\text{Length of the best direction vector}}{\text{number of unit vector for the best direction vector}} \tag{24}$$

The electrons with many scattering has less MSG value (Fig. 42).

As reconstruction goodness and energy dependence of the direction distribution, the cut criteria was decided as in Table 3

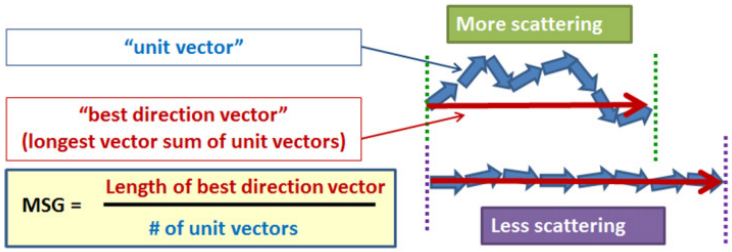

Figure 42: The schematic view of MSG calculation.

Table 3: Solar cut criteria. Cossun is the cosine of the angle to the sun.

Energy(MeV)	MSG	Cossun
19-20	-	0.93
18-19	< 0.4	0.45
	0.4-0.5	0.77
	0.5-0.6	0.81
	> 0.6	0.91
17-18	< 0.4	0.35
	0.4-0.5	0.61
	0.5-0.6	0.73
	> 0.6	0.73
< 16	< 0.4	-0.11
	0.4-0.5	0.29
	0.5-0.6	0.37
	> 0.6	0.65

6.9 Pre/Post Activity Cut

We select events with a single charge peak in the gate window to remove events from low energy muons.

The electron events decayed from the muon with some energy are removed by 50 μs time difference cut. However, 50-μs cut, which uses the time difference to the LE triggered event, can not remove events from the parent muons with lower energy than the threshold of the LE trigger. These events can be detected by the prompt γ, a few μs before the candidate. The prompt γ is produced with the muon at the interaction of cosmic ray and the atmosphere.

Sometimes, the low energy muons themselves seem like the neutrinos because they have similar Cherenkov angle. These muons decay in the detector and the electron is observed after the main peak.

The width of the event gate window is 40 μs, 5 μs before the trigger and 35 μs after. Because the lifetime of the muon is 2.2 μs, 35 μs is enough. In the gate window, the peak of the number of PMT hits within a 15 nsec(N_{15}) sliding window are searched. When an event has more than 12 hits peak before the trigger or 15 hits peak after trigger, the event is removed. If a candidate event has SLE only triggered event within the 40 μs gate and the distance between candidate event and SLE event is less than 500 cm, that candidate event is removed.

6.10 μ/π Cut

Though most of the muon and pion events are removed by the pion cut or Cherenkov angle cut, a few events/year survive. Because these events deposit large energy along a short track, they have more charge in one PMT. From the number of hit PMTs in a 50 ns time window (N50) and the sum of the charge of those PMTs (Q50), the average charge per PMT (Q50/N50) is calculated. If $Q50/N50 > 2.0 + 0.0025 \times energy$, then that event is removed.

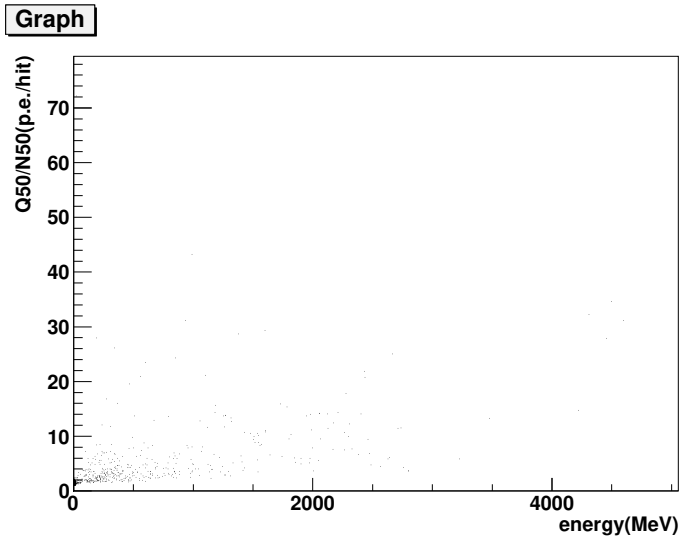

Figure 43: The distribution of Q50/N50 as a function of the reconstructed energy.

6.11 N16 cut

When the low energy muon is captured by ^{16}O, ^{16}N is produced. ^{16}N decays with a half-life 7.13 sec and emits γ and/or electron. To remove this γ or electron events, the correlation with the stopping muons are searched. If there is a stopping muon between 100 μs to 30 s before the candidate and that muon vertex is within 250 cm from the candidate vertex, that candidate event is removed.

6.12 Cherenkov Angle Cut

The Cherenkov angle cut removes low energy muons produced by atmospheric ν_μ and multiple gamma-ray events which are often caused by neutral current interactions of atmospheric neutrinos. The electron at SK energy range is relativistic. Its Cherenkov

angle is 42°. The interaction of atmospheric neutrinos and oxygen produces multiple γ. A multiple γ event looks to have large Cherenkov angle. As muons are non-relativistic, they have smaller Cherenkov angle. The cut criteria is the Cherenkov angle be less than 38° (μ-like) or larger than 50° (γ-like).

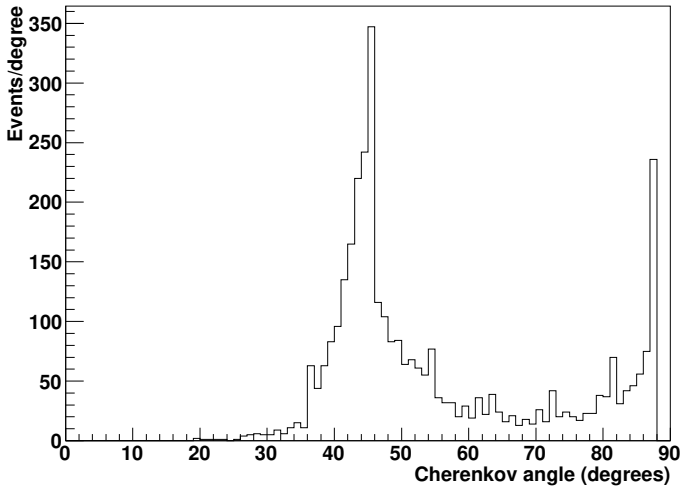

Figure 44: Cherenkov angle distribution.

6.13 Summary of Reduction Efficiency

To estimate the reduction efficiency, mono-energetic events were generated by MC simulation. The generated events distribute uniformly in the 32 kton FV.

The random sample (Sec. 6.3) is used for the spallation cuts and N16 cut, because they need the correlation to proceeding muons.

The efficiency summary of each reduction steps is shown in Table 4. The total efficiency was calculated as

$$\text{total efficiency} = \frac{\text{number of survived events through all cuts}}{\text{number of generated events in 22.5 kton}}. \quad (25)$$

Thus, the efficiency is normalized by the size of the fiducial volume. The total efficiency for the events in the 22.5 kton fiducial volume is shown in Fig. 45.

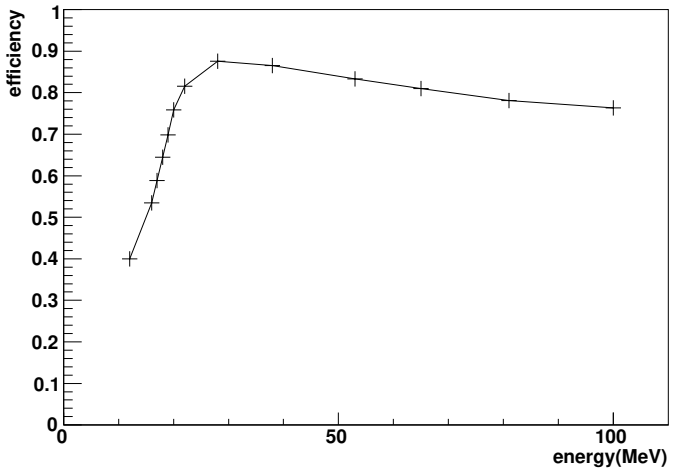

Figure 45: Total reduction efficiency.

Table 4: Reduction efficiency.

Reduction	Data	Efficiency							Efficiency method
		12MeV	17MeV	19MeV	22MeV	38MeV	65MeV	80MeV	-
First reduction	1.7×10^{-4}	0.62	0.67	0.67	0.67	0.67	0.67	0.67	MC
Spallation cut	0.11	0.85	0.87	0.90	0.95	1.0	1.0	1.0	random
Gamma cut	0.84	0.93	9.94	0.94	0.97	0.98	0.98	0.98	MC
Pion cut	0.84	0.98	0.99	0.99	0.99	0.98	0.96	0.96	MC
OD correlated event cut	-	1.0	1.0	1.0	1.0	1.0	1.0	1.0	MC
Multi ring cut	-	1.0	0.99	0.99	0.99	0.99	0.98	0.98	MC
Solar event cut	0.91	0.64	0.80	0.91	0.99	1.0	1.0	1.0	MC
Pre/post activity cut	0.95	1.0	1.0	1.0	1.0	1.0	1.0	1.0	random
μ/π cut	0.96	1.0	1.0	1.0	1.0	0.96	0.91	0.88	MC
N16 cut	0.94	1.0	1.0	1.0	1.0	1.0	1.0	1.0	random
Cherenkov angle cut	0.55	0.9	0.94	0.95	0.95	0.97	0.98	0.98	MC

7 Results of GRB neutrino searches

In this section, we analyze the data after the reduction in Sec. 6 and show the result.

In Sec. 7.1, neutrinos correlated with a GRB were searched for in the time windows for each GRB. The time window is fixed to ±500 sec in Sec. 7.1.1. In Sec. 7.1.2, the start and end time for each GRB is read from the GRB database and used as the start/end time for the analysis time window. The significance of the number of events in the time window to the expected background is discussed.

In Sec. 7.2, the excess from the background was searched for by stacking the data of 2208 GRBs. The fluence limit for 1 GRB average was calculated.

7.1 Neutrino Search for Individual GRB

7.1.1 ±500 sec Analysis

GRBs with more neutrino events than expected background are searched for. Among ±1000 sec reduction data, the inner 1000 sec (±500sec) is used as a search window and outer 1000 sec (-1000∼-500 sec, +500∼+1000 sec) are used for background estimation (Fig. 46).

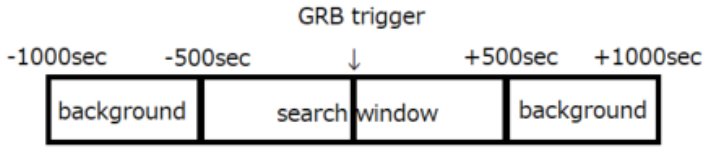

Figure 46: The signal window and background window around a GRB event. The GRB trigger time is the time from the GRB database (Sec. 6.1).

The search window was decided from the time scale of models and from the effect of neutrino mass. For a core collapse supernovae, the neutrino luminosity is expected to decrease in ∼10 sec and to be within 1 sec from explosion[43, 50]. For neutron star mergers, neutrino emission is expected to continue a few tens of msec after merging[35]. In Ref. [10], a cosmic string model is thought to be better suited to describe the short GRB population. The neutrino emission time from gamma emission is less than ∼10 sec for these three models.

Assuming neutrinos and gamma-rays are emitted at same time, neutrino detection

is delayed by

$$\frac{1}{2}\left(\frac{m_\nu}{E_\nu}\right)^2 \times (\text{gamma-ray} \quad \text{time-of-flight}). \tag{26}$$

The combination of observations of the cosmic microwave background (CMB), baryon acoustic oscillations, and CMB lensing limits the sum of neutrino masses to $\leq$ 0.23 eV. From the mass differences measured by neutrino oscillation experiments, the maximum mass is less than 0.087 eV. The delay of 8 MeV neutrino from z=8.2 is $\sim$24 sec. Conservatively, a $\pm$500 sec search window is selected.

No previous GRB neutrino search was done in SK-IV and the background rate in the detector may change during the 10 years of SK-IV running. The number of events in the time window around a search window (Fig. 46) was checked. The number of events after the first reduction and spallation cut for each GRB and its distribution is shown in Fig. 47 and Fig. 48. Most of the events after the spallation cut are events from cosmic rays, solar neutrinos, and surrounding rocks. The rate of these events is stable and the histogram becomes a Poisson distribution. Because Fig. 48 is consistent with a Poisson distribution, the time variation of backgrounds in the detector is negligible. The sum of the background window is used as the background sample.

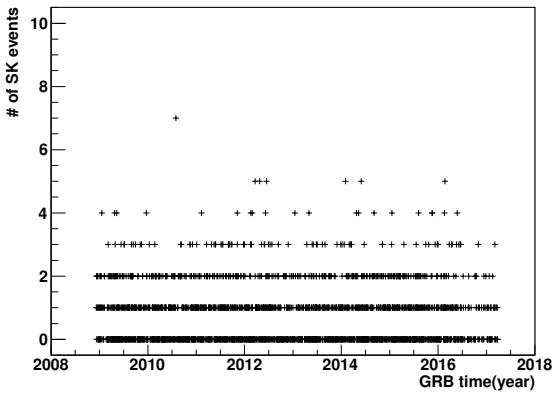

Figure 47: Number of events in the background window for each GRB after the spallation cut.

Fig. 49 shows a distribution of the number of events in each GRB after all reduction cuts are applied. For 2208 GRBs, 251 events remain in the background window after reduction. The background rate for 1 GRB is 251/2208=0.114 events/GRB. In Fig. 49, the red line shows number of GRBs that have a specific number of SK events in the search window. The black line shows expected number of Poisson distribution with an average of 0.114 and 2208 samples.

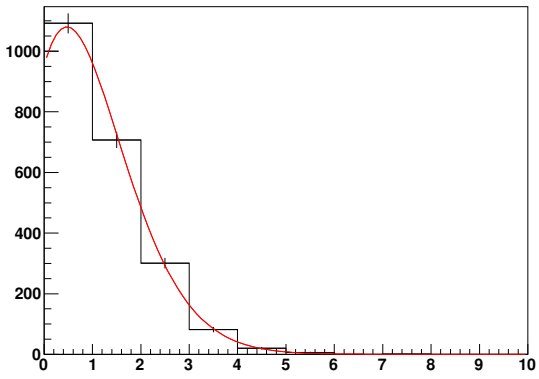

Figure 48: Distribution of the number of events in the background window after spallation cut.

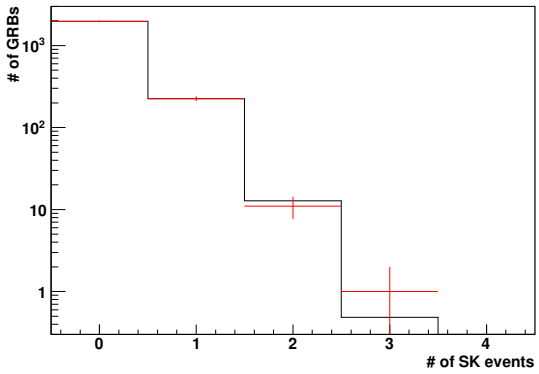

Figure 49: Number of SK events within ±500 sec around a GRB trigger. The black line shows the expected number with the estimated background rate. Red points are the observed numbers.

The distribution of the observed number of events is consistent with background. However, as shown in Fig. 49, 3 events remain in search window for a GRB. The GRB with 3 SK events, 140616A is listed in Table 50. The energy and time difference from the remaining 3 SK event is shown in Fig. 50. These events can be spallation events. The energy is in the spallation region (Sec. 6.3). The time, traversal distance, and longitudinal distance from the most likely parent muon is small (Table 5).

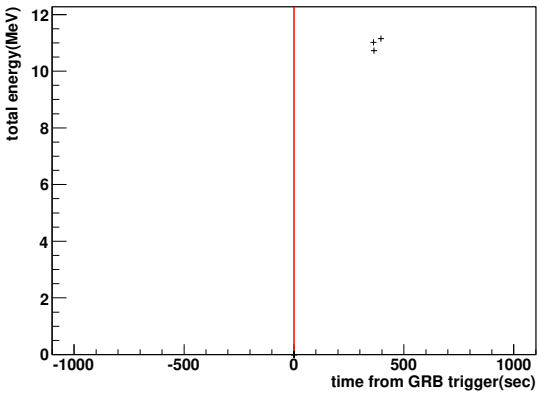

Figure 50: The SK events around GRB140616A.

Energy (MeV)	Time difference (sec)	Traversal distance (m)	Longitudinal distance (m)
11.0	0.41	2.5	-6.6
10.7	0.66	2.9	-3.3
11.2	0.44	1.9	-7.5

Table 5: The status of the SK events around GRB140616A.

7.1.2 t1-t2 analysis

A GRB duration is distributed from 0.01 sec to 1000 sec (Fig. 51). If the neutrino emission period is related to this duration, it would be better for reducing backgrounds to limit the time window to the GRB duration time rather than opening a fixed time window like the analysis in the previous sub-section. The number of SK events (N_{ev}) observed from the GRB start time (t1) to end time (t2) were counted (Fig. 52). There are 2194 GRBs with t1 and t2 available in the database.

The estimated number of background events in a t1-t2 window is 0.114events/2000 sec.$\times$ $(t2-t1)$. The probability of N_{ev} in t1-t2 is calculated from a Poisson distribution of

this expected background (<0.114). The probability distribution is shown in Fig. 53. The most "rare" event is GRB130315A. This GRB has 2 SK events in a time width of 271 sec and the probability is 0.00046.

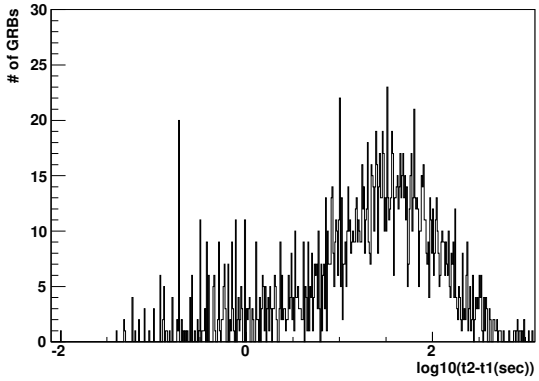

Figure 51: The distribution of t2-t1.

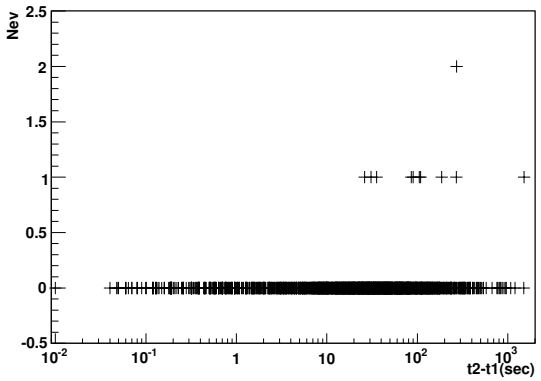

Figure 52: N_{ev} versus t1-t2 width.

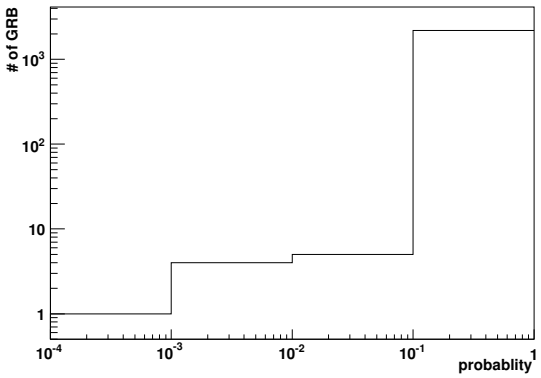

Figure 53: The probability of N_{ev} in t1-t2.

The consistency of Fig. 53 was estimated by toy Monte-Carlo (MC) simulation. One MC set is calculated as follows.

- For a GRB, the number of SK events in ±1000 sec, N_{2000}, is determined from a Poisson distribution of the background rate, 0.114 event/2000 sec.
- N_{2000} time differences from the GRB trigger time are randomly allocated ($\Delta t_1, \Delta t_2, ..., \Delta t_{N_{2000}}$).
- Δt_i in the t1-t2 window is counted. This is N_{ev} for a GRB.

- The probability of N_{ev} is calculated as in the data analysis.
- Repeat the above process for 2194 GRBs (where t1 and t2 data is available) and make the probability distribution.

From 10,000 sets of MC, the importance of "rare" events is evaluated. In the data, 1 GRB has N_{ev} of probability less than 0.001 and 5 GRBs less than 0.01. 25.7% of MC sets have 1 or more GRBs of probability less than 0.001 (Fig. 54). 60.5% of MC sets have 5 or more GRBs of probability less than 0.01 (Fig. 55). The data is consistent with the background.

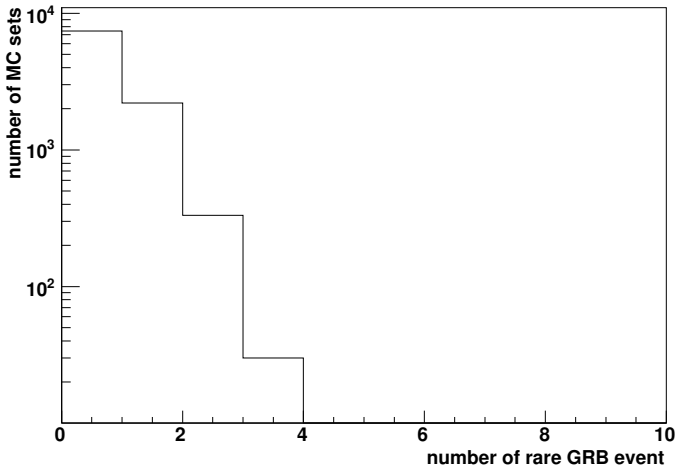

Figure 54: Number of MC sets with GRBs of toy MC probability less than 0.001.

7.2 Stack Analysis

As described in the previous sections, no obvious excess of events was observed for each individual GRB. It can be understood that the expected number of events at SK is much smaller than a single event and cannot be detected in the individual GRB search. However, an excess could be seen by accumulating SK data for many GRBs. We call this method the "stack analysis". Fig. 56 shows the time variation of SK events based on the GPS trigger time. In Fig. 56, no obvious excess around GRB triggers is seen. The background sample is -1000 to -500 sec and 500 to 1000 sec from the GRB trigger times (total 25.6 days). The energy distribution shown in Fig. 57 is consistent with the background.

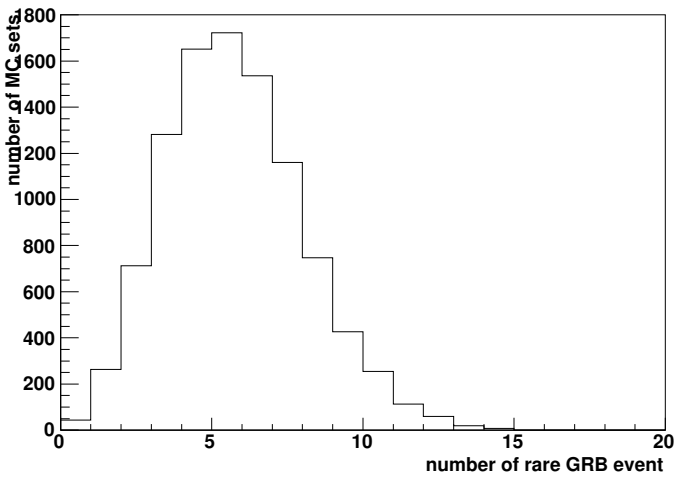

Figure 55: Number of MC sets with GRBs of toy MC probability less than 0.01.

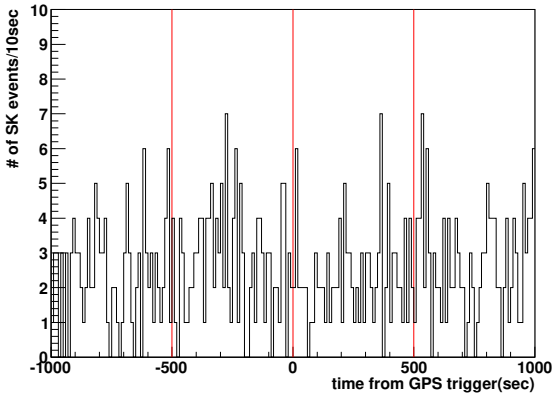

Figure 56: Number of stacked SK events per 10 sec from GRB trigger times.

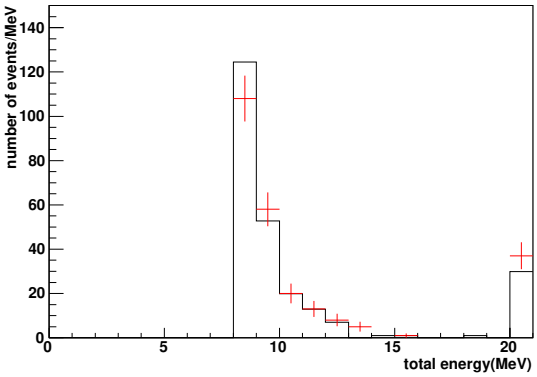

Figure 57: Energy distribution of observed data (red) and background (black). The 21 MeV bin includes events above 20 MeV.

7.2.1 Fluence Limit Calculation

Since no excess was seen, the fluence limit was calculated from the stacked data in the following way[19]. Using a Poisson distribution with the background rate, N_{90}, the 90% C.L. limit on the number of neutrino events in the search window can be calculated as

$$\int_{N_{bg}}^{N_{90}} dx\ \text{Poisson}(N_{obs}, x) = 0.9 \int_{N_{bg}}^{\infty} dx\ \text{Poisson}(N_{obs}, x),$$
$$\text{Poisson}(N_{obs}, x) = \frac{\exp(-x)x^{N_{obs}}}{N_{obs}!} \tag{27}$$

where N_{bg} is the expected number of background events, N_{obs} is the number of observed events and Pisson(N_{obs}, x) is the poisson probability for N_{obs} events with mean of x. When N_{bg} is expected and N_{obs} is observed, the probability that the number of neutrino events is less than N_{90}, is 90%. For limit calculation, the events of 8-100 MeV are counted. Without the events above 100 MeV, N_{bg} is 221 and N_{obs} is 218. From $N_{obs} = 218$, $N_{bg} = 221$, N_{90} is 23.9.

Then, the fluence limit Φ can be calculated by the equation,

$$\Phi = \frac{N_{90}}{N_T \int dE_\nu \lambda(E_\nu)\sigma(E_\nu)\epsilon(E_e)}, \tag{28}$$

where N_T is the number of target nuclei in the SK 22.5 kton fiducial volume, λ is the neutrino spectrum normalized to unity, σ is the total neutrino cross section as a function of neutrino energy, and ϵ is the detector efficiency. The neutrino spectrum λ is assumed to be flat in this thesis. The cross-section σ by Strumia and

Vissani [49] was used. The neutrino energy and the positron energy has a relation of $E_e = E_\nu - 1.293\ MeV$ (Sec. 5.2). The efficiency is calculated by applying the reduction (Sec. 6) to the MC sample (Sec. 5) or random sample. Since the MC sample was generated in the 32 kton inner detector volume, the efficiency for the calculation is the one normalized to the 22.5 kton fiducial volume from the 32 kton efficiency in Fig. 45.

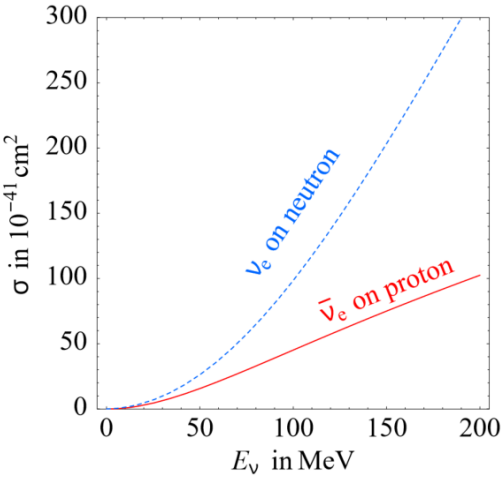

Figure 58: The total cross-sections of quasi-elastic scattering. Figure from [49].

The fluence limit from 8 MeV to 100 MeV for all 2208 GRB is 1.03×10^8 cm^{-2}.

The fluence limit as a function of energy is also calculated. The energies selected are 8, 15, 28, 38, 53, 65, and 80 MeV to divide the whole energy range in a log scale. To see the effect of the energy threshold, a 10 and 12 MeV sample are added.

As observed events or background events, the events in the limited energy around the target energy are counted. The energy range for each target energy is determined as following.

First, the MC sample of that energy is made. The event vertex in the detector and direction is decided randomly. Cherenkov light generation, propagation and the detector response is simulated.

Then, the data reduction is applied to the sample and the energy distribution is fitted with a Gaussian to get the peak (E_{peak}) and the RMS of the energy distribution (σ). 3 σ around E_{peak} is the energy range. For example, Fig. 59 is the energy distribution after reduction of the 28 MeV sample. The energy peak is 28.02 MeV. 2.89 MeV is the deviation and 19.35-36.69 MeV is the energy range. Table 6 shows the energy peak and the RMS for the each MC energy and Table 7 shows the N_{90}

and the fluence limit.

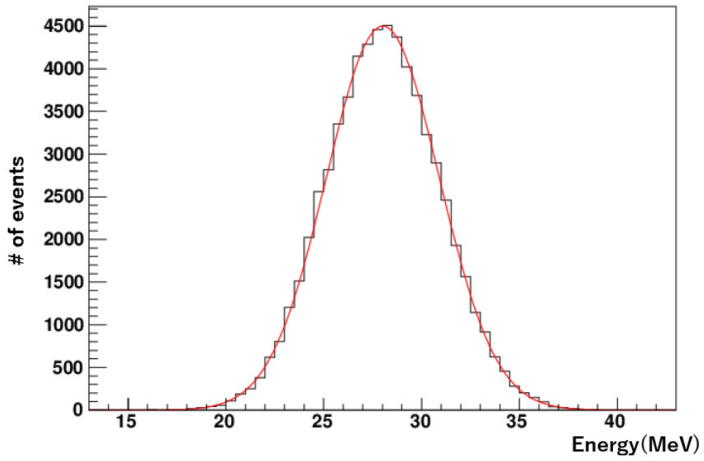

Figure 59: The energy distribution of the 28 MeV MC sample after reduction.

The background events in the 25.6 days sample is too small for the samples above 38 MeV. The background sample was enlarged to the normal data taking period from December 2008 to March 2017 without ±1000 sec around GRBs. The livetime is 2826 days. The numbers of expected events around each energy is shown in Table 7.

The 4 events of 38 MeV and 53 MeV are the same events. Their energies are 41.7 MeV (GRB100911A), 44.8 MeV (GRB110801A), 47.4 MeV (GRB150127C), and 41.5 MeV (GRB150301A). The 1 event in the 65 MeV and 80 MeV samples is 75.4 MeV around GRB130509A.

The limit for all GRBs is listed in Table 7. The limits for 1813 long GRBs / 323 short GRBs are also calculated from the number of observed events around long/short GRBs and the background ratio is the same for all GRBs. Table 8 and Table 9 show number of observed events, number of expected background events, N_{90}, and the neutrino fluence limit for long and short GRBs. From Fig. 6 in Sec. 1.3, we compare this limit to the limit of the previous SK study and limit from Borexino. Fig. 60 shows the neutrino fluence upper limit per GRB. This study gives the best limit at 28 MeV to 80 MeV. In the previous SK study, the fluence limit as a function of energy is the limit on monoenergetic neutrinos at specific energies (E'_ν). Therefore the energy range and N_{90} is same for all energy point. The efficiency at those energies ($\epsilon(E'_\nu)$) were calculated by MC simulation of the monoenergetic neutrino events. With this efficiency, the fluence limit was obtained by replacing $\lambda(E'_\nu)$ in eq. 28 by a delta function $\delta(E_\nu - E'_\nu)$. The limit of the previous SK study is still better under 20 MeV due to its wide energy range (7-80 MeV).

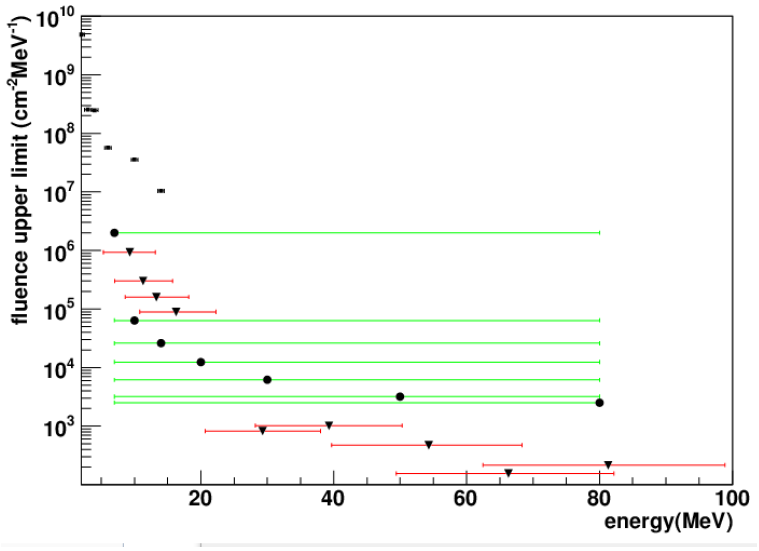

Figure 60: The fluence limt per GRB per MeV. Width of the marker is the energy range of the limit calculation. Red is this study. Green is the previous SK study [28]. In the previous SK study, energy range of events were same for all the data points and are indicated with the horizontal bar. The detector efficiency was estimated by simulations assuming a monochromatic neutrino energy indicated by the filled circle. Black is Borexino study [22].

Positron energy (MeV)	Energy peak after reduction (MeV)	RMS (MeV)
8	7.94	1.31
10	10.07	1.45
12	12.10	1.60
15	15.25	1.91
28	28.02	2.89
38	37.97	3.68
53	52.71	4.78
65	64.50	5.47
80	79.38	6.07

Table 6: The relation of MC energy and reconstructed energy.

Neutrino energy (MeV)	# of observed event	# of expected event	N_{90}	Fluence limit (cm^{-2})
9.23±3.93	198	210	18.6	1.62×10^{10}
11.36±4.35	212	219	21.5	5.75×10^{9}
13.39±4.80	213	220	21.6	3.40×10^{9}
16.54±5.73	80	67	26.9	2.27×10^{9}
29.31±8.67	0	0	2.30	3.14×10^{7}
39.26±11.04	4	1.78	6.28	4.98×10^{7}
54.0±14.34	4	1.59	6.44	2.99×10^{7}
65.79±16.41	1	1.06	3.25	1.12×10^{7}
80.67±18.21	1	0.90	3.31	1.73×10^{7}

Table 7: The 90% C.L. of number of event and the fluence limit for 2208 GRBs.

Positron energy (MeV)	# of observed event	# of expected event	N_{90}	Fluence limit (cm^{-2})
9.23±3.93	152	172	13.2	1.15×10^{10}
11.36±4.35	161	180	14.2	3.78×10^{10}
13.39±4.80	162	181	14.3	2.25×10^{9}
16.54±5.73	59	55.0	16.6	1.15×10^{9}
29.31±8.67	0	0	2.30	3.14×10^{9}
39.26±11.04	3	1.47	5.32	4.22×10^{7}
54.0±14.34	3	1.31	5.44	2.53×10^{7}
65.79±16.41	1	0.87	3.32	1.15×10^{7}
80.67±18.21	1	0.74	3.38	1.77×10^{8}

Table 8: The 90% C.L. of number of event and the fluence limit for 1813 long GRBs.

Positron energy (MeV)	# of observed event	# of expected event	N_{90}	Fluence limit(cm^{-2})
9.23±3.93	41	30.7	19.9	1.73×10^{10}
11.36±4.35	45	32.0	22.9	6.11×10^{9}
13.39±4.80	45	32.2	22.8	3.58×10^{9}
16.54±5.73	18	9.80	15.0	1.31×10^{9}
29.31±8.67	0	0	2.30	3.14×10^{7}
39.26±11.94	1	0.26	3.67	2.91×10^{7}
54.0±14.34	1	0.23	3.69	1.71×10^{7}
65.79±16.41	0	0.16	2.30	7.93×10^{6}
80.67±18.21	0	0.13	2.30	1.20×10^{7}

Table 9: The 90% C.L. of number of event and the fluence limit for 323 short GRBs.

8 Summary and Outlook

8.1 Summary

Neutrinos associated with GRBs were searched for in the SK detector. GRBs are one of the most luminous astronomical objects ever observed. By the improvement of satellites and ground telescopes, some features of GRBs are observed. However, no models are confirmed as the mechanism for GRBs. Neutrino observation will help to study the mechanism.

Until now, no clear neutrino signal is observed with GRBs. In the previous stack study of SK, neutrinos for 1454 GRBs in the SK-I period were searched for. In this study, 2208 GRBs from Dec. 2008 to Mar. 2017 is the target. After reduction, 250 events remain in the search window, $\pm$500 sec around each GRB trigger time, while the background rate is 0.114 events/1000 sec. No obvious excess was seen in the time development of the number of events and energy distribution of the combined data.

Three or less SK events are detected in the $\pm$500 sec window for individual GRBs. Three SK events around GRB140616A may be spallation events because their vertex and timing is near the most likely parent muons.

Considering the neutrino emission period that is related to the gamma duration, we tried a new analysis method as follows. The number of SK events between GRB start/stop time (N_{ev}) was also studied. The probability that a GRB has N_{ev} or more SK events was calculated for each GRB. The distribution of this probability was evaluated by toy MC simulation. The timing of SK events were randomly allocated and a distribution of the probability was generated. In this study, the data is consistent with the background. Though no obvious signal is observed, the fluence limit was calculated from stacked data. The limit from 8 MeV to 100 MeV for all 2208 GRB is 1.03×10^8 cm^{-2}. The flat spectrum was assumed. The limit per GRB is 5.07×10^5 cm^{-2}. The redshift of 189 GRBs were observed and the average is z = 1.8. The expected fluence from a cosmic string model at this distance is $\sim 10^7 - 10^8$ cm^{-2}. The mechanism for most GRBs is not the cosmic string model.

The limit as a function of energy is calculated. MC events are generated and reductions are applied for typical energies. In the energy distribution after reduction, the energy peak $\pm 3\sigma$ was set as the energy range for each energy. The events in the energy range are counted as signal or background. Then, the limit is calculated to be 1.5×10^5 cm^{-2}/MeV/GRB at 12 MeV. In this study, the limits for long GRBs and short GRBs are calculated. The better efficiency of SK-IV and the large statistics gives a better fluence limit between 28 MeV to 80 MeV.

8.2 Outlook

A new phase of SK, SK-Gd[9] will start soon. In SK-Gd, 0.2% gadolinium sulfate $Gds(SO_4)_3$ will be added to the SK water in order to identify $\bar{\nu}_e$ events. The identification of $\bar{\nu}_e$ is useful for the detection of supernova relic neutrinos and the direction of supernova bursts. Gadolinium captures a neutron from inverse beta decay and emits gamma rays of ∼8 MeV total energy (Fig. 8.2).

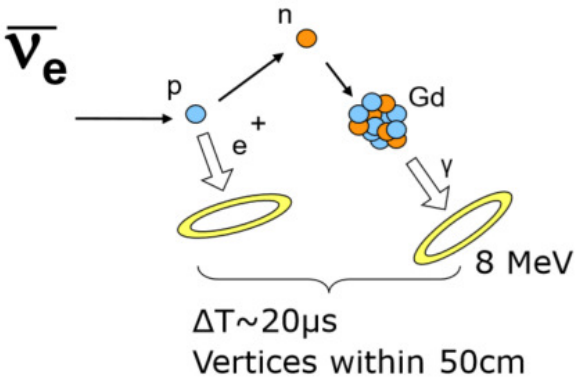

Figure 61: Neutron tagging with gadolinium. Figure from Ref. [47].

Supernova relic neutrinos are the accumulated neutrinos of the supernovae that have been occurring since the beginning of the universe. The background rate for the relic neutrino search can decreased by detecting the coincidence of positron signals and delayed gammas from protons that capture neutrons. The detection of this 2.2 MeV gamma-ray with Cherenkov light has a low efficiency to clearly distinguish from the background. On the other hand, 8 MeV gamma-rays from gadolinium that captures neutrons can be detected with Cherenkov light. The cross-section of neutron capture by gadolinium is about 5 orders of magnitude larger than that of proton.

The effect of dissolving gadolinium in the SK water was studied by an R&D project called EGADS. $Gd_2(SO_4)_3$ is dissolved into a 200 m^3 tank like a small SK tank. A selective water filtering system which removes impurities except for gadolinium has been developed. The neutron capture efficiency and impact to the water transparency was studied. The EGADS experiment determined a target concentration of $Gd_2(SO_4)_3$ to be 0.2%.

In the current study, the dominant backgrounds are spallation events below ∼20 MeV and decay electron events from invisible muons by atmospheric neutrino above that. Most of the spallation processes emit neutrons and will be removed by neutron tagging. $^{9}_{3}$Li is a possible radioactive isotope produced by the cosmic ray muons that emits neutrons and electrons above the energy threshold. The backgrounds by spallation will become small and neutral current events will be the dominant background. The expected background rate is ∼2 events/year. The decay electron events do not emit neutrons and the background will become $sim1/4$. The fluence limit of 10 years SK-Gd observation can be estimated by substituting expected background rate and detector efficiency of 80% to Eq. 28. The limit is expected to become ∼1/6 below 15 MeV and ∼1/2 above 28 MeV.

References

[1] *ATM-3 (ATLAS Muon TDC Version 3) User's Manual*.

[2] Cern program library long writeup w5013. 1994.

[3] B. P. Abbott *et al*. Gw170817: Observation of gravitational waves from a binary neutron star inspiral. *Phys. Rev. Lett.*, 119:161101, Oct 2017.

[4] K. Abe *et al*.. Solar neutrino measurements in super-kamiokande-iv. *Phys. Rev. D*, 94:052010, Sep 2016.

[5] S. Adrian-Martinez et al. First search for neutrinos in correlation with gamma-ray bursts with the ANTARES neutrino telescope. *JCAP*, 1303:006, 2013.

[6] S. Adrian-Martinez et al. Search for muon neutrinos from gamma-ray bursts with the ANTARES neutrino telescope using 2008 to 2011 data. *Astron. Astrophys.*, 559:A9, 2013.

[7] Juan A. Aguilar. Online gamma-ray burst catalog for neutrino telescopes. 2011.

[8] John N. Bahcall and Peter Mészáros. 5–10 gev neutrinos from gamma-ray burst fireballs. *Phys. Rev. Lett.*, 85:1362–1365, Aug 2000.

[9] John F. Beacom and Mark R. Vagins. Antineutrino spectroscopy with large water Čerenkov detectors. *Phys. Rev. Lett.*, 93:171101, Oct 2004.

[10] V. Berezinsky, B. Hnatyk, and A. Vilenkin. Gamma ray bursts from superconducting cosmic strings. *Phys. Rev. D*, 64:043004, Jul 2001.

[11] K. S. Cheng, Yun-Wei Yu, and T. Harko. High-redshift gamma-ray bursts: Observational signatures of superconducting cosmic strings? *Phys. Rev. Lett.*, 104:241102, Jun 2010.

[12] E. R. Davies. *Machine Vision: Theory, Algorithms, Practicalities, Academic Press*, 1997.

[13] A. G. Vieregg *et al*.. The first limits on the ultra-high energy neutrino fluence from gamma-ray bursts. *The Astrophysical Journal*, 736(1):50, 2011.

[14] A. Morel *et al*.. Analysis of variations in ocean color1. *Limnology and Oceanography*, 22:709–722, 1977.

[15] A. Suzuki *et al*. Improvement of 20 in. diameter photomultiplier tubes. *Nuclear Instruments and Methods in Physics Research Section A: Accelerators, Spectrometers, Detectors and Associated Equipment*, 329(1):299 – 313, 1993.

[16] B. Aharmim *et al*.. A search for astrophysical burst signals at the sudbury neutrino observatory. *Astroparticle Physics*, 55:1 – 7, 2014.

[17] Bing Zhang *et al*.. Physical processes shaping gamma-ray burst x-ray afterglow light curves: Theoretical implications from the swift x-ray telescope observations. *The Astrophysical Journal*, 642(1):354, 2006.

[18] D. Band *et al.*. Batse observations of gamma-ray burst spectra. i - spectral diversity. *Astrophysical Journal, Part 1*, 413(1):281–292, 1993.

[19] E. Thrane *et al.*. Search for neutrinos from grb 080319b at super-kamiokande. *The Astrophysical Journal*, 697(1):730, 2009.

[20] F. De Paolis *et al.*. High energy neutrinos from grbs. *Nuclear Physics B - Proceedings Supplements*, 100(1):347 – 349, 2001.

[21] K. Asakura *et al.*. Study of electron anti-neutrinos associated with gamma-ray bursts using kamland. 806(1):87, 2015.

[22] M. Agostini *et al.*. Borexino's search for low-energy neutrino and antineutrino signals correlated with gamma-ray bursts. *Astroparticle Physics*, 86:11 – 17, 2017.

[23] M.Nakahata *et al.*. Calibration of super-kamiokande using an electron linac: The super-kamiokande collaboration. *Nuclear instruments and Methods in Physics Research Section A: Accelerators, Spectrometers, Detectors and Associated Equipment*, 421(1):113–129, 1999.

[24] S. Briggs *et al.*. Observations of grb 990123 by the compton gamma-ray observatory. *The Astrophysical Journal*, 524, 1999.

[25] S. Fukuda *et al.*. The super-kamiokande detector. *Nuclear Instruments and Methods in Physics Research Section A: Accelerators, Spectrometers, Detectors and Associated Equipment*, 501(2):418 – 462, 2003.

[26] William S. Paciesas *et al.*. The fourth batse gamma-ray burst catalog (revised). *The Astrophysical Journal Supplement Series*, 122(2):465, 1999.

[27] Gerald J. Fishman and Charles A. Meegan. Gamma-ray bursts. *Annual Review of Astronomy and Astrophysics*, 33:415–458, 1995.

[28] S. Fukuda et al. Search for neutrinos from gamma-ray bursts using Super-Kamiokande. *Astrophys. J.*, 578:317–324, 2002.

[29] D. Guetta, M. Spada, and E. Waxman. On the neutrino flux from gamma-ray bursts. *Astrophys. J.*, 559:101, 2001.

[30] Nishino H. *et al.*. High-speed charge-to-time converter asic for super-kamiokande detector. *Nulear Instruments and Methods in Physics Reserach Section A: Accelerators, Spectrometers, Detectors and Associated Equipment*, 610(3), 2009.

[31] F. Halzen and G. Jaczko. Signatures of γ ray bursts in neutrino telescopes. *Phys. Rev. D*, 54:2779–2783, Aug 1996.

[32] David Alexander Kann, S. Klose, and A. Zeh. Signatures of extragalactic dust in pre-swift grb afterglows. *Astrophys. J.*, 641:993–1009, 2006.

[33] J. I. Katz and T. Piran. Persistent counterparts to gamma-ray bursts. *The Astrophysical Journal*, 490(2):772, 1997.

[34] K.Bays. *Search for the diffuse supernova neutrino background at super-kamiokande*. PhD thesis, University of California, Irvin, 2011.

[35] Kenta Kiuchi, Yuichiro Sekiguchi, Koutarou Kyutoku, and Masaru Shibata. Gravitational waves, neutrino emissions, and effects of hyperons in binary neutron star mergers. *Class. Quant. Grav.*, 29:124003, 2012.

[36] M. M. Kochkarov *et al.*. Search for low-energy neutrinos from gamma-ray bursts at the baksan underground scintillation telescope. *Physics of Particles and Nuclei*, 46(2):197–200, Mar 2015.

[37] P. Kumar. Gamma-ray burst energetics. 523(2):L113, 1999.

[38] Peter Meszaros. Gamma-Ray Bursts. *Rept. Prog. Phys.*, 69:2259–2322, 2006.

[39] M.Ikeda. *Precise measurement of solar neutrinos with super-kamiokande iii*. PhD thesis, University of Tokyo, 2009.

[40] M.Malek. *A search for supernova relic neutrinos*. PhD thesis, State University of New York at Stony Brook, 2003.

[41] M.Shiozawa. *Search for proton decay via $p \to e^+\pi^0$ in a large cherenkov detecotr*. PhD thesis, University of Tokyo, 1999.

[42] P. Mszros and M. J. Rees. Multi-gev neutrinos from internal dissipation in gamma-ray burst fireballs. *The Astrophysical Journal Letters*, 541(1):L5, 2000.

[43] Ken'ichiro Nakazato, Kohsuke Sumiyoshi, Hideyuki Suzuki, Tomonori Totani, Hideyuki Umeda, and Shoichi Yamada. Supernova neutrino light curves and spectra for various progenitor stars: From core collapse to proto-neutron star cooling. *The Astrophysical Journal Supplement Series*, 205(1):2, 2013.

[44] A. Orii. Development of new data acquisition system at super-kamiokande for nearby supernova bursts. In *Proceedings, 34th International Cosmic Ray Conference (ICRC 2015): The Hague, The Netherlands, July 30 - August 6, 2015*, 2016.

[45] Re'em Sari, Tsvi Piran, and Ramesh Narayan. Spectra and light curves of gamma-ray burst afterglows. *The Astrophysical Journal Letters*, 497(1):L17, 1998.

[46] S.Desai. *High energy neutrino astrophysics with super-kamiokande*. PhD thesis, Boston University, 2004.

[47] Hiroyuki Sekiya. Supernova neutrinos in sk-gd and other experiments. *Journal of Physics: Conference Series*, 888:012041, 09 2017.

[48] Michael Smy. Low Energy Event Reconstruction and Selection in Super-Kamiokande-III. In *Proceedings, 30th International Cosmic Ray Conference (ICRC 2007): Merida, Yucatan, Mexico, July 3-11, 2007*, volume 5, pages 1279–1282, 2007.

[49] Alessandro Strumia and Francesco Vissani. Precise quasielastic neutrino/nucleon cross-section. *Physics Letters B*, 564(1):42–54, 2003.

[50] T. Totani, K. Sato, H. E. Dalhed, and J. R. Wilson. Future detection of supernova neutrino burst and explosion mechanism. *The Astrophysical Journal*, 496(1):216, 1998.

[51] Mario Vietri. The soft x-ray afterglow of gamma-ray bursts; a stringent test for the fireball model. *The Astrphysical Journal Letters*, 478(1):L9, 1997.

[52] Eli Waxman. High energy neutrinos from gamma-ray bursts. *Nuclear Physics B - Proceedings Supplements*, 91(1):494 – 500, 2001. Neutrino 2000.

[53] Eli Waxman and John Bahcall. High energy neutrinos from cosmological gamma-ray burst fireballs. *Phys. Rev. Lett.*, 78:2292–2295, Mar 1997.

[54] Y.Zhang. *Experimental Studies of Supernova Relic Neutrinos at Super-Kamiokande-IV*. PhD thesis, Tsinghua University, 2015.

[55] Z.Conner. *A study of solar neutrinos using the super-kamiokande detector*. PhD thesis, University of Maryland, 1997.